CHARACTERIZATION, ANALYSIS AND SIMULATION OF

FINE COAL FILTRATION

by

Joel Alejandro Mejia

A thesis submitted to the faculty of
The University of Utah
in partial fulfillment of the requirements for the degree of

Master of Science

Department of Metallurgical Engineering

The University of Utah

August 2013

The University of Utah Graduate School

STATEMENT OF THESIS APPROVAL

The thesis of   **Joel Alejandro Mejia**

has been approved by the following supervisory committee members:

Jan D. Miller	, Chair	**June 10, 2013**
		Date Approved
Chen-Luh Lin	, Member	**June 10, 2013**
		Date Approved
Raj K. Rajamani	, Member	**June 10, 2013**
		Date Approved

and by   **Jan D. Miller**   , Chair of

the Department of   **Metallurgical Engineering**

and by Donna M. White, Interim Dean of The Graduate School.

ABSTRACT

Fine coal filtration and dewatering are of great importance to the coal industry due to the significant impact in the quality, shipping, and handling of clean coal. High moisture content in the clean coal product reduces its heating value, increases costs, and reduces the coke yield in the case of metallurgical coal. In this regard, it is of significant importance to improve our fundamental understanding of water removal from the pore network structures present in filtration cakes. This thesis research presents the results obtained from the analysis regarding fluid flow through packed particle beds such as those occurring during filtration in an effort to expand the studies of particle characterization and its influence on coal dewatering. The study shows the importance of high resolution x-ray microtomography (HRXMT) as an important analytical tool for the three-dimensional study of particle beds.

The multiphase flow and dewatering that occurs during fine coal filtration is described, and important factors that influence the efficiency of filtration, including the particle size distribution, pressure drop, shape, and wetting characteristics of the coal particles are considered. The experiments are designed to simulate the process of coal filtration using the Lattice-Boltzmann methodology, and identify the conditions that lead to the improved water removal and moisture reduction. The thesis and research reported

herein demonstrate how HRXMT and the Lattice-Boltzmann Method (LBM) can help in the short-term prediction and understanding of water removal from the pore network structures present in coal filtration cakes.

Based on the analysis of HRXMT images, it is shown that the pore network structure has a significant influence on the retention of water in the filter cake. Narrow capillaries were found in the filter cakes with hydrophilic particles, while wider capillaries were mostly found in the filter cakes with hydrophobic particles. In addition, tests with different pressure drops were performed. Although the pore network structure analysis showed that the capillaries were narrower at higher initial pressures, the increase in pressure drop decreased the amount of water retained in the filter cake. The pressure drop increase helped overcome the capillary forces that retain the water in the filter cakes.

This project is dedicated to my family whose words of encouragement keep me going, for their moral support, patience, and understanding. To my professors and mentors, Dr. Miller and Dr. Lin, for believing in me, for their motivation, and encouragement to reach my goals.

"Basta un poco de espíritu aventurero para estar siempre satisfechos, pues en esta vida, gracias a Dios, nada sucede como deseábamos, como suponíamos, ni como teníamos previsto." – Noel Clarasó

"Just a little adventurous spirit is enough to be always satisfied, because in this life, thank God, nothing happens as we wanted, as we supposed, or as we had planned." - Noel Clarasó

TABLE OF CONTENTS

LIST OF TABLES

LIST OF FIGURES

LIST OF SYMBOLS

A	Cross-sectional area
Bo	Bond number
C_d	Drag coefficient
Ca	Capillary number
D	Dimensions of the system
D_ρ	Density parameter used to define contact angle in He model
DdQq	Lattice model with d dimensions and q vector velocities
dP/dx	Pressure gradient along the x-direction
f_i	Particle distribution function in the direction i of the lattice
f^N	Particle distribution function with N number of particles
g	Gravity
inHg	Inches of mercury
k	Permeability constant
$\bar{k}$	Surface tension constant parameter in He model
L	Length
lu	Lattice units
ℓ	Thickness of porous media
M	Viscosity ratio

N	Number of particles in the distribution function
$P*$	Pore entry pressure
p	Fluid pressure
p_{nw}	Pressure of the nonwetting fluid
p_w	Pressure of the wetting fluid
p_c	Capillary pressure
Q	Volume flow rate
R	Radius
Re	Reynolds number
$r*$	Radii of curvature
S_w	Saturation of the wetting fluid phase
S_{0w}	Irreducible wetting fluid saturation
S_{nw0}	Residual nonwetting saturation
U	Fluid velocity
u	Macroscopic velocity
V	Volume of the fluid
v_w	Characteristic velocity of the wetting fluid
v	Unit cell volume
Δp	Pressure difference
$xBody$	Body force applied in the x-direction
γ	Interfacial tension
γ_{lg}	Interfacial tension between liquid and gas phase

γ_{sg}	Interfacial tension between solid and gas phase
γ_{sl}	Interfacial tension between solid and liquid phase
μ	Dynamic viscosity of the fluid
μ_w	Dynamic viscosity of the wetting fluid
μ_{nw}	Dynamic viscosity of the nonwetting fluid
v	Kinetic fluid viscosity
ρ	Density of the fluid
ρ_l	Density of the liquid
ρ_g	Density of the gas
ρ_w	Density of the wetting fluid
ρ_{nw}	Density of the nonwetting fluid
τ	Relaxation time
Ω	Collision integral

ACKNOWLEDGEMENTS

CHAPTER 1

INTRODUCTION

Fine coal filtration and dewatering are of great importance to the coal industry due to its significant impact on the quality, shipping and handling of the coal product. Filtration of fine coal involves filter cake formation and removal of surface moisture by drawing air through the porous structure. An accurate assessment of the transport properties in porous media is of major importance in the development of improved filtration processes (Leonard & Hardinge 1991; Wakeman, & Tarleton 2005; Tien 2006). Currently, there is limited understanding of the fundamental phenomena involved at the pore scale level which controls the average behavior of the filtration process.

There are several factors that affect the final moisture content of a coal filter cake, including cake thickness, pressure drop across the cake, drying time, viscosity of the liquid, surface tension of the liquid, filter media, particle size distribution, permeability of the cake, specific gravity of dry solids, inherent moisture of dry solids, type of filter and construction, and volume of air or gas pulled through the cake per unit of time per unit area, among others (Leonard & Hardinge, 1991). Other factors may include particle shape and wetting characteristics (Asmatulu & Yoon, 2012; Yoon et al., 2006). Understanding each factor and their relationship is necessary to define the optimal conditions for coal dewatering during the filtration process.

However, such a task is complicated and overwhelming since it entails a large group of variables, including the complexity of the pore geometry, which is often tedious to determine experimentally. The approach currently used involves a series of simplified assumptions in order to obtain a mathematical relationship between a small group of variables, making the decision and design process simpler. Nonetheless, there is no linear or nonlinear rule for a combination of the effective physical properties from the microscopic scale that can be used to predict the macroscopic scale properties. The lack of fundamental understanding at the pore scale level during the coal filtration process limits the ability to predict and resolve common operational problems such as cake cracking and moisture retention. In this regard, it is important to introduce appropriate experimental techniques and theoretical models to describe in detail at the pore scale level the flow occurring through a packed bed of coal particles during filtration.

Understanding the fundamental parameters involved in the filtration process is essential in order to improve the water removal and define the condition for minimum cake moisture content. To gain better understanding of the complex transport phenomena that occur in the porous media, the effect of three-dimensional pore geometry on the effective transport properties of the filter cake is in progress. X-ray microtomography is being used for the characterization of the complex three-dimensional pore geometry by direct digitalization of the real pore network structure of the coal cake. The system, shown in Figure 1.1, is the high resolution x-ray microtomography (HRXMT) from Xradia (2009), which employs an x-ray detector with submicron resolution combined with a microfocus x-ray source. In this way, with a voxel resolution of about 1 micron, the real pore network structure of the coal cake composed of coal particles with a size
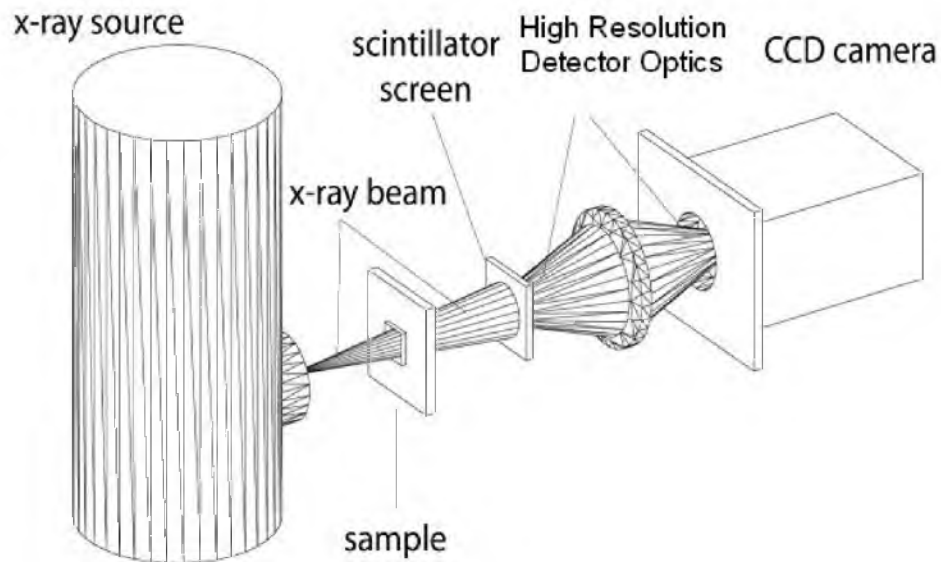
Figure 1.1: Xradia's High-Resolution X-ray Microtomography (HRXMT), the MicroXMT-400, uses a microfocus x-ray source with 150 kV accelerating voltage. The sample can be translated in x-y-z-theta directions with a high-resolution stage. High resolution is achieved with a proprietary x-ray detector with an effective detector pixel size < 1 micron.

less than 20 mesh (0.85 mm) can be described. The use of HRXMT and emerging Lattice-Boltzmann simulation methods provides a foundation to explore such matters. The simulation study relies on a combination of three-dimensional (3D) data, obtained from HRXMT measurements, and the Lattice-Boltzmann Model (LBM) to generate a model and describe the conditions for improved water removal during filtration.

In view of the foregoing, an extensive research program has been designed to study fine coal filtration using HRXMT and LBM for fluid flow simulation in order to help identify optimum conditions of operation. This is the continuation of research developed by Professors J.D. Miller and C.L. Lin at the University of Utah using LBM in 3D problems in order to improve the understanding of the phenomena associated with

fluid flow in packed particle beds (Lin et al., 2010). This thesis includes results from a set of lab experiments under controlled and reproducible conditions that have been carried out to evaluate the simulation results, and to verify the application of this emerging technology in the study and analysis of filtration processes.

1.1 Review of Literature

The combination of x-ray microtomography and fluid dynamics modeling can be of great relevance in mineral processing, and in particular in dewatering processes. X-ray microtomography has the capabilities of characterizing the complex geometry of the pore network structure created in the filter cake after filtration. On the other hand, LBM can be used to model the flow of multiphase fluid mixtures through very complicated geometries. Both techniques can provide a graphic representation of multiphase simulations and help determine the conditions to improve water removal during filtration operations. The 3D porous structures captured by HRXMT analysis are coupled with the LBM to simulate and to establish a fundamental relationship between pore microstructure and filtration operation variables.

1.1.1 X-Ray Microtomography

X-ray tomographic imaging is, in general terms, an x-ray-based method by which radiation of an opaque sample in different directions allows for its 3D reconstruction (Lin et al., 2010). The development of this noninvasive technique is recent but it has had a huge impact in several areas of science. In fact, the first device capable of producing true reconstructed images was developed by G. N. Hounsfield in 1972 at EMI in England

called Mark I (Isherwood, 2004). This prototype was based, in part, on mathematical methods developed by A. M. Cormack (1977) a decade earlier.

The mechanics of x-ray tomography testing is relatively simple. The sample is located between the x-ray source and the detector (Figure 1.1). Then the sample is illuminated in different directions, and for each direction the projection of the attenuation coefficients is measured. When the x-rays interact with the solids in the sample, the photons may be absorbed, scattered, diffracted, refracted, or simply transmitted through the medium. As the x-rays pass through the solid particles, the x-rays are attenuated, or weakened, following the Lambert-Beer's law (Wildenschild & Sheppard, 2013). When the attenuation values are high, the x-ray beam is highly "attenuated," or weakened, as it passes through highly dense materials. On the other hand, when the material is relatively less dense, low attenuation numbers are produced indicating that the material is practically transparent to the beam.

Therefore, it is assumed that those voxels with minimum attenuation values are the voxels where void spaces are present due to the absence of highly dense particles. These attenuation coefficients also depend on the beam density, bulk density of the material, atomic electron density (Wildenschild & Sheppard, 2013). In order to obtain an accurate description of the material it is necessary to have sufficient variation in the attenuation coefficients. Because of this, the object or sample must be rotated so that different radiographic projections can be collected at different angles, obtain a full distribution of attenuation coefficients, and finally back-calculate those coefficients to reconstruct the image (Wildenschild & Sheppard, 2013).

The reconstruction of the samples is based on a mathematical formalism known as the Radon transform and its mathematical framework. After processing, the x-ray computed tomography produces a spatial description of the object under analysis where the field of view is divided in elemental digital units known as voxels. The voxel, or volumetric pixel, is a volume element representing a value in a three-dimensional space (Novelline, 1997). Each voxel is characterized by the attenuation coefficient of the material of which it is composed. This spatial digital characterization of the sample under analysis allows for further digital processing of the sample.

Figure 1.2 shows a packed bed of coal particles and its porous network structure as obtained by the HRXMT system at the University of Utah (Lin et al., 2010). The particle size is 500 x 850 μm, the resolution of each voxel is 5.62 μm in length, and the size of the image is 400 x 400 x 800 voxels. It is possible to observe how image processing of the digital data allows for a clear separation between the solid and the air of the pore network structure due to the distinct difference in attenuation coefficients. This technique easily obtains the porous network of the packed particle bed. Obtaining these images is of great importance in order to simulate fluid flow through the porous network formed by the void space created within the packed bed of particles. During simulation the fluid flows through this network structure having a specific connectivity with well-defined pore dimensions not only to determine the local flow but also the overall permeability of the sample. However, due to the complex geometry of the network structure, it is important to consider LBM simulations since this method has the ability to compensate for complex boundaries of arbitrary geometries.
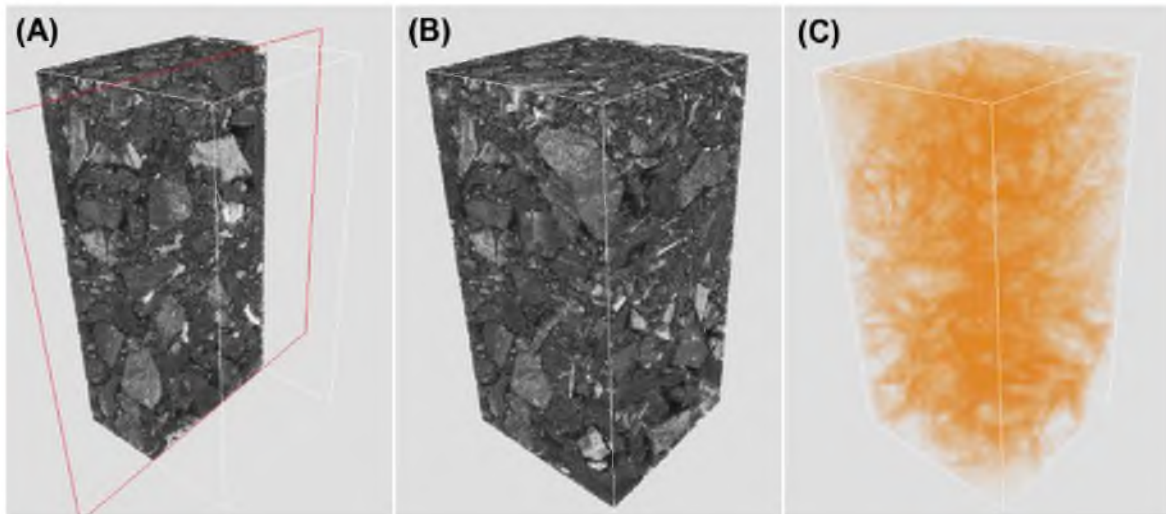
Figure 1.2: 3D image reconstruction of a packed bed of coal particles (500 x 850 μm). The voxel resolution is 5.62 μm and the image size is 400 x 400 x 800 voxels. (A) shows the cutoff view of the CT reconstructed packed particle bed, (B) shows the complete CT reconstructed packed particle bed, and (C) shows the pore network structure.

1.1.2 The Lattice-Boltzmann Method (LBM)

LBM evolved from the original lattice gas cellular automata model (LGCA), in which space, time, and particle velocities in the simulation are all discrete. This means that the model excludes continuously varying quantities and related notions, and includes objects that have distinct, separated values (Sukop & Thorne, 2006). In the LGCA model, the space was discretized in a regular arrangement on a lattice and a set of Boolean variables (having one of two values: true or false) (Frish et al., 1986). Within the lattice, each algorithmic entity occupies a position and describes the population of particles at each node and its interaction (described as molecular direction) with its identical neighbors (Rothman & Zaleski, 1997). However, the use of different, irregular, lattice geometries led to the development of the LBM since the LGCA showed some difficulties related to the lack of Galilean invariance, anomalous velocity dependency of the fluid

pressure and statistical noise when using irregular geometries (Succi, 2001). It was discovered that instead of using a discrete particle, a density distribution could be beneficial since it eliminated the noisiness and allowed for a more general collision operator.

The LBM method is regarded as one of the simplest microscopic "particle" approaches to modeling macroscopic dynamics. The LBM evolved from the LGCA in order to overcome the problems with different scenarios, but keeping the streaming and collision principles. The fundamental difference between the two models is that LBM replaced the Boolean variable by a particle distribution function (PDF), f_i, neglecting individual particle motion, which eliminated the statistical noise problem presented by the LGCA (Succi, 2001). The LBM is based on the Boltzmann transport equation for the time rate of change of the particle distribution function in a particular state. The Boltzmann equation simply says that the rate of change is the number of particles scattered into that state minus the number scattered out of that state (Chen, 1993).

The images of the porous structures of packed particle beds in Figure 1.2 reveal why the LBM method is more suitable for this kind of problem than the standard computational fluid dynamics (CFD) mesh methods, such as finite elements or finite volume method. The standard solution with a CFD solver requires the construction of a grid, the definition of the boundary conditions at the boundary nodes, and the solution of the Navier-Stokes equation at each node (Lin et al., 2010). The standard CFD methodology, therefore, would require an enormous amount of time for grid construction and computer simulation.

1.1.3 The LBM and Multiphase Simulations

The classical approach (Tiller, 1975; Dahlstrom and Silverblatt, 1977; Svarosvsky, 1990) for filtration analysis is based on Darcy's law, an empirical equation that describes one-dimensional fluid flow through uniform incompressible porous media. Knowledge of cake pore microstructure and its correlation to macroscopic cake properties is required to model the filtration from a fundamental point of view. The single component, single phase Lattice-Boltzmann (LB) model has been used as a common tool to study transport phenomena through pore space (Lin & Miller, 2004 and cited references; Videla, Lin & Miller, 2007). Moreover, the LBM is a class of computational fluid dynamics (CFD) used to model the flow of multiphase fluid mixtures through very complicated geometries. The LB is increasingly attracting researchers in many areas from turbulence flow to multiphase flow in porous media. Appendix A describes the permeability derived for the LBM in a single component single-phase simulation, which is the foundation for multiphase LBM simulations.

In order to improve the water removal and define the condition for minimum cake moisture content, a multiphase LB fluid flow model is required to investigate the flow through the porous media. Several Lattice-Boltzmann multiphase fluid flow models have been introduced in the past years finding applications in different areas of fluid dynamics such as phase separation (Rothman & Zaleski, 1991), and fingering phenomena in a channel (Kang et al., 2004) among others. The major advantage claimed for pursuing the use of LBM instead of standard CFD methods resides in its ability to model complex solid boundaries in any arbitrary geometry, a scheme suitable for code parallelization and

ability to incorporate microscopic force interactions that control the interface dynamics (Lin et al., 2010).

In general, the LBMs for multiphase flow can be described as single component or multicomponent models. Single component models describe phase separation by an equation of state that under the critical temperature automatically segregates phases into two stable densities, vapor (light density) and liquid (heavy density). In this category we found the single component Shan and Chen model (1993), single component free-energy model, and the He-Shan-Doolen model (1998) to be of interest. On the other hand, multicomponent models use one particle distribution function (PDF) and one evolution equation to represent each fluid component in the system and segregation is simulated by interaction between the two independent fluids. For further discussion and comparison of these methods the reader is referred to the work done by Chen and Doolen (1998) and He and Doolen (2002).

In his seminal work, He et al. (1999) presents a new multiphase model derived directly from discretizing the continuous kinetic equation for non-ideal fluids modified for incompressible flow. As mentioned previously, the He-Chen-Zhang (1999) model is an extension of the He-Shan-Doolen model (1998). The model has not been used extensively and is not as popular as the Shan and Chen model. Videla (2009) has applied the model to 2D and 3D Rayleigh-Taylor instability simulations (He et al., 1999; Zhang et al., 2000) and compared the data with theoretical values and results from another CFD simulation showing good qualitative and quantitative agreement.

Unlike the traditional CFD methods that resolve the macroscopic governing equations using a free boundary surface approximation, the He-Chen-Zhang model

(1999) simulates the interfacial dynamics, such as phase segregation and surface tension, from mesoscopic kinetic equations. In this model the interfacial dynamics are the result of molecular interactions where two distributions functions are used, one for tracking the pressure and velocity, and another for tracking only the density. When the molecular attraction is strong enough, the fluid automatically segregates into two different phases. One of the major advantages with respect to the Shan and Chen model (1993) is that the surface tension in the He model can be adjusted beforehand as a free parameter due to its thermodynamic consistency. Appendix B illustrates the derivation of the physics of multiphase flow in porous media using single component multiphase LBM for this study.

1.2 Preliminary Work

Some preliminary exploratory work was done using HXRMT and the LBM. The LBM allows for the quantitative description of fluid flow through a porous network structure in a packed bed of particles (Lin et al., 2010). The solid-fluid interaction can be simulated when the pore network structure is provided from the HRXMT data. The following paragraphs describe preliminary work performed using the principles of HRXMT and LBM.

1.2.1 Permeability

In a previous study, a team of researchers at the University of Utah performed different experiments to determine the permeability through a packed bed of particles using HRXMT and Lattice-Boltzmann simulations (Lin et al, 2010). From the 3D reconstructed HRXMT image shown in Figure 1.2, the pore structure for the packed bed

of coal particles was determined and used for this study. The voxel size for this data set was 5.62 μm. Figure 1.3 illustrates the 3D view of the LB simulated flow through the pore space of the packed particle bed. The velocity scale is color-coded and shown on the right side. The red color represents a high velocity profile while the blue color represents slow velocity. Velocity ranges from black for no flow, through blue, green, yellow and finally red for the highest flow rate. The image on the left illustrates the solid particle phase as revealed by the HXRMT. The image on the right side illustrates the pore network structure as the solid particle phase is removed. This clearly shows the nature of the flow channels. These images were used to compute permeability by modeling Stokes flow in both the simulated pore space of a packed bed and actual 3D digital pore space from HRXMT analysis using the LB method. The calculation of permeability in this study was 9.28×10^{-8} cm^2.
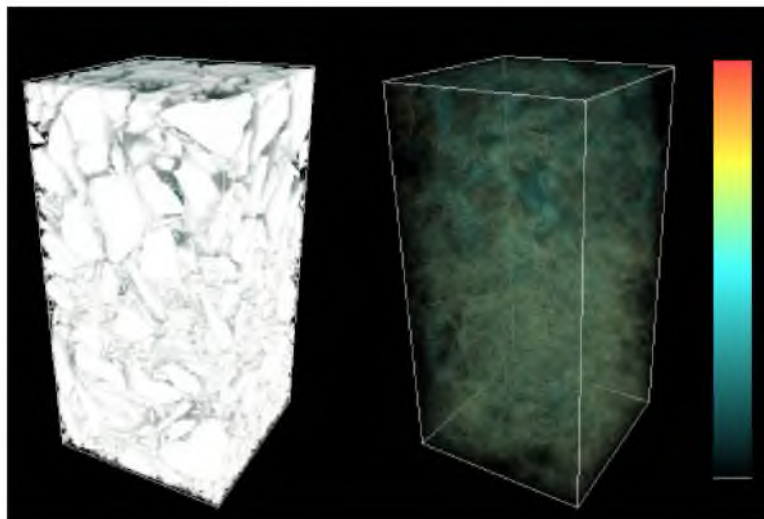
Figure 1.3: 3D views of LB simulated flow through a packed bed of coal particles (500 x 850 μm). The voxel resolution is 5.62 μm and the image size is 400 x 400 x 800 voxels. Left hand side image with white solid phase and right hand side image with solid phase removed. Color-coded bar shows the solution velocity ranges from black for no flow to red for the highest flow rate.

1.2.2 Capillarity

The solid-fluid interaction explained before can be extended to the analysis and simulation of two-phase flow in complex porous structures. The two-phase flow refers to the combination of liquid and gaseous phases involved in the simulation. To show this phenomenon, the behavior of the LBM in simple capillary tubes is illustrated below.

In a capillary tube, there is fluid displacement when the flow is driven by a difference in pressure strong enough to overcome the capillary pressure. Figure 1.4 shows LBM simulated results for capillary tubes where the nonwetting fluid displaces the wetting fluid, also known as drainage process. The figure, from left to right, shows the nonwetting fluid as it displaces the wetting fluid. This two-phase interaction simulation was performed at different driving pressures. The LBM simulation was carried out using a D2Q9 model, which is a 2-dimensional model that contains 8 velocities and 1 rest particle (Sukop & Thorne, 2006). It is the simplest model that can be implemented on the concepts of single component, single-phase model. In this case, the size of the lattice was 35 x 130 squared lattice units (lu^2).

The previous example shows a simple D2Q9 simulation regarding only one capillary tube. However, the capillary phenomenon of interest involving the network microstructure of the filter cake requires two or more capillary tubes (throats) to be present. Moreover, these capillary tubes must be of different sizes in order to appropriately represent the network structure in the packed bed of particles. The D2Q9 simulation illustrates in Figure 1.5 shows the simplest case of two-phase flow of two pores of different diameters under the same pressure difference.
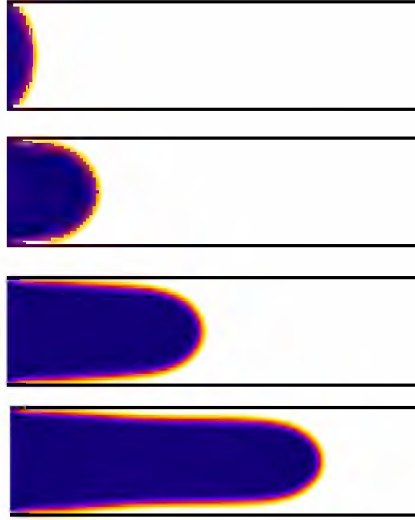
Figure 1.4: Simulations of fluid displacement for increasing difference in pressure controlled by the density at the outlet, which has values from top to bottom: 0.2508, 0.2498, 0.2482, and 0.2466. D2Q9 lattice of size 35 x 130 lu^2. Parameters for simulations are $\bar{k}$ = 0.1, D$_\rho$ = 0.99, and $\rho_l/\rho_g = 10$.
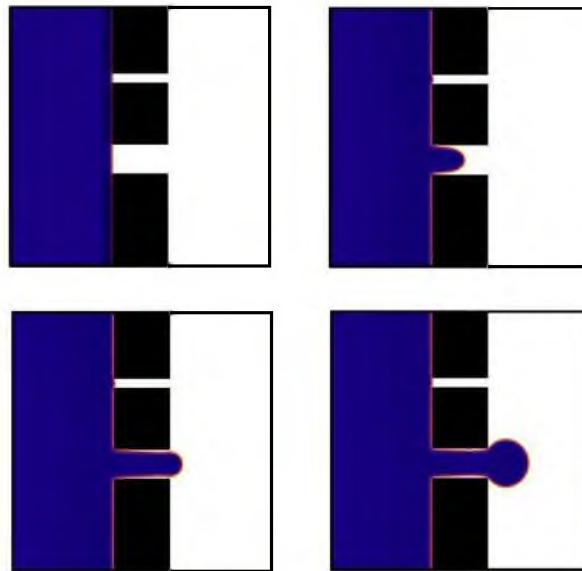
Figure 1.5. Simulations of fluid displacement in a capillary tube with two throats of different radius. From left to right and top to bottom image: flow after 1,000, 10,000, 20,000, and 30,000 iterations. D2Q9 lattice of size 35 x 130 lu^2. Parameters for simulations are $\bar{k}$ = 0.1, D$_\rho$ = 0.99, and $\rho_l/\rho_g = 10$.

In order to simulate the differences in diameter of the capillary tubes, a new simulation with different throat sizes was performed using a modified He-Chen-Zhang model. As Figure 1.5 shows, one of the throats is six times smaller than the other and, therefore, has a six times higher entry pressure. The pressure across the phases in the simulation has been set in such a way that the value is higher for the entry pressure at the bigger diameter throat, but smaller than the entry pressure for the smaller diameter throat. In Figure 1.5 it is possible to observe the preferential flow that is developed by the meniscus, which invades the channel with the higher throat radius having a smaller flow resistance. In conclusion, it is evident that this modified He-Chen-Zhang model has good qualitative agreement with theory for two-phase flow in porous media (Videla, 2009). Therefore, it can be applied to a porous network structure such as the one formed by a packed bed of particles.

1.2.3 Network Simulations

Lenormand et al. (1988) ran numerous network simulations and experiments performed in transparent etched networks to identify patterns and describe percolation of a non-wetting fluid when injected into a medium saturated with a wetting fluid (Videla, 2009; Lin et al., 2010). As an outcome of his research, he proposed a phase diagram for immiscible displacement characterized by the capillary number (Ca) and the viscosity ratio (M) as shown in Figure 1.6. The diagram shows the existence of three basic domains for fluid penetration: stable displacement, viscous fingering, and capillary fingering. In the stable displacement region, the major force is due to viscosity interaction of the injected fluid. The flow shows a flat front moving towards the exit with some

irregularities with the dimensions of a few pore scales. In the viscous fingering region the major force is due to viscosity interaction of the displaced fluid. In this type of flow, the displaced fluid spreads across the porous network towards the exit. On the other hand, the capillary fingering region is characterized by a major force due to capillarity and exhibits a tree-like fingering effect growing in all directions, even toward the entrance-forming loops. These loops trap the displaced wetting fluid leading to a higher final saturation than the viscous fingering. This model was later expanded for the simulation of filtration in an actual 3D image of a packed bed of coal particles as obtained from x-ray microtomography (XMT) analysis.
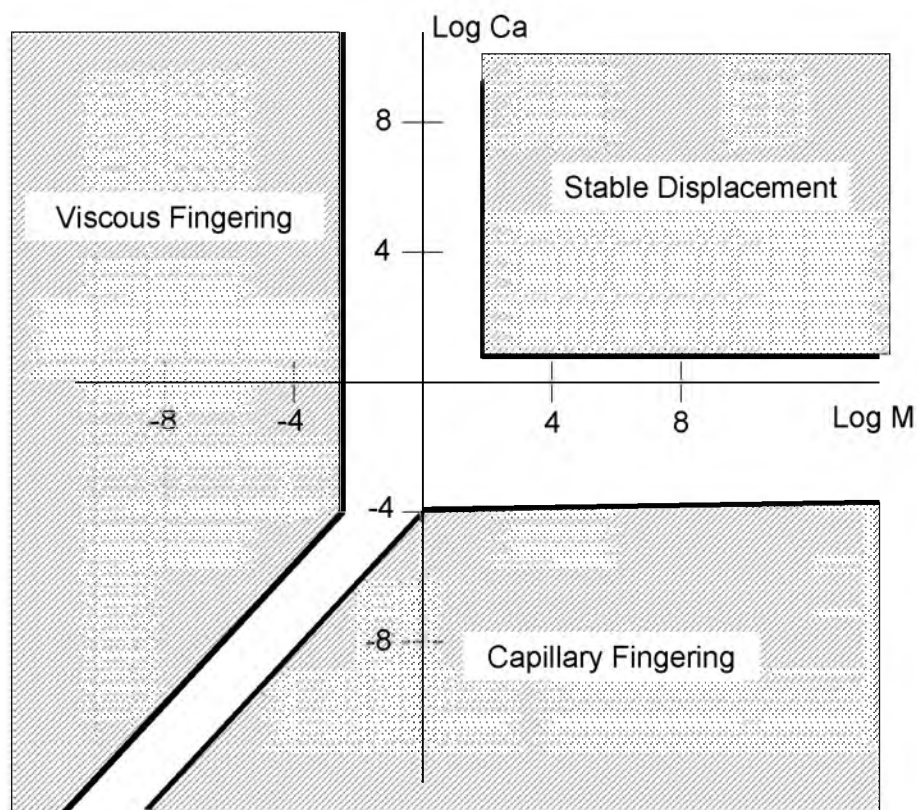
Figure 1.6: Lenormand Diagram. (Adapted from Lenormand et al., 1988).

Figure 1.7 shows 2D simulations of the interface advance explained before by using the He-Chen-Zhang model (1999) applied to a packed bed of sand particles where the pore network structure has been captured by XMT analysis. In this simulation a two-dimensional XMT image slice has been used and flow goes from top to bottom, induced by a fixed pressure difference. Parameters of simulation in Figure 1.7 are set in such a way to obtain a flow in the transition zone between capillary fingering and stable displacement as described by Lenormand et al. (1988). The capillary number, Ca, is 6.77×10^{-2} and the density ratio, M, is 3. The images show displacement of the wetting fluid by the nonwetting fluid. The sequence of images starts with complete saturation and show the displacement of the wetting fluid in the network structure. The wetting phase passes through the coarse pore diameters easily due to the less resistant paths, but leaves residual wetting phase trapped in the very small pore spaces with a high-flow resistance. The wetting phase also gets trapped due to the lack of the higher pressure needed to displace the fluid. This is representative of Lenormand et al. (1988) pattern similar to capillary fingering.

Figure 1.8 shows a comparison of the same structure shown in Figure 1.7 with a new 2D simulation condition where the surface tension, $\bar{k}$, is varied. Comparison at the same level of iteration shows that the percolation follows the same pattern for both multiphase flow in porous media simulations for this porous network structure. This is probably due to the fact that both simulations are run with the same pressure gradient and therefore the path of least resistance has not changed. However, reduction of the surface tension produces longer and thinner fingers.
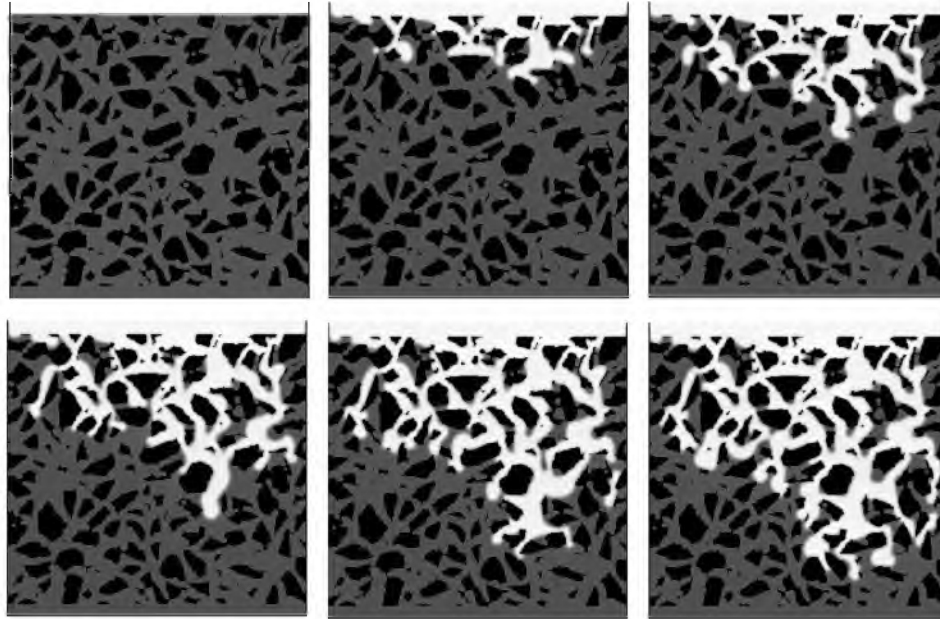
Figure 1.7: Sequence of simulations of two-phase flow in a packed bed of sand particles. Percolation simulations by the single component He-Chan-Zhang LBM. For a density ratio = 3.0 and Ca = 6.77x10^{-2}. Lattice size of 256 x 256. Images show increments of 5,000 iteration steps each.
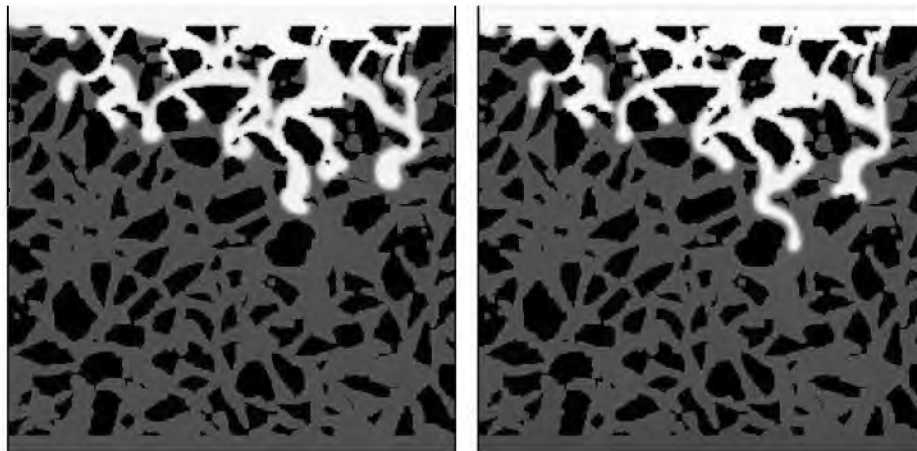
Figure 1.8: Two different simulations for the same density ratio = 3.0 and pressure gradient but different surface tension. Left image has a high surface tension ($\bar{k}$ = 0.1, Ca = 6.77x10^{-2}) and right image has a low surface tension ($\bar{k}$ = 10^{-5}, Ca = 230). Both images were taken after 10,000 iterations. Parameter $\bar{k}$ defines the surface tension.

Figure 1.9 shows another comparison between the 2D simulations in Figure 1.8 for a simulation where the density ratio has been inverted. The image on the left shows the control simulation and the image to the right shows the experimental condition. In this new case, the low-density fluid displaces the heavier fluid and the pattern of flow changes since the pressure field has changed. According to the Lenormand diagram (Figure 1.6), a stronger viscous fingering type of flow is expected with more and longer fingers being formed due to the stronger viscous interaction and interface front instability. As the comparison shows, fingering is formed in zones of low resistance to flow and once formed they start growing rapidly towards the exit. In conclusion, application of the single component multiphase flow LBM known as the He-Chen-Zhang model (1999), coupled with XMT analysis to define the complex pore geometry, allows for simulation of flow in porous media.
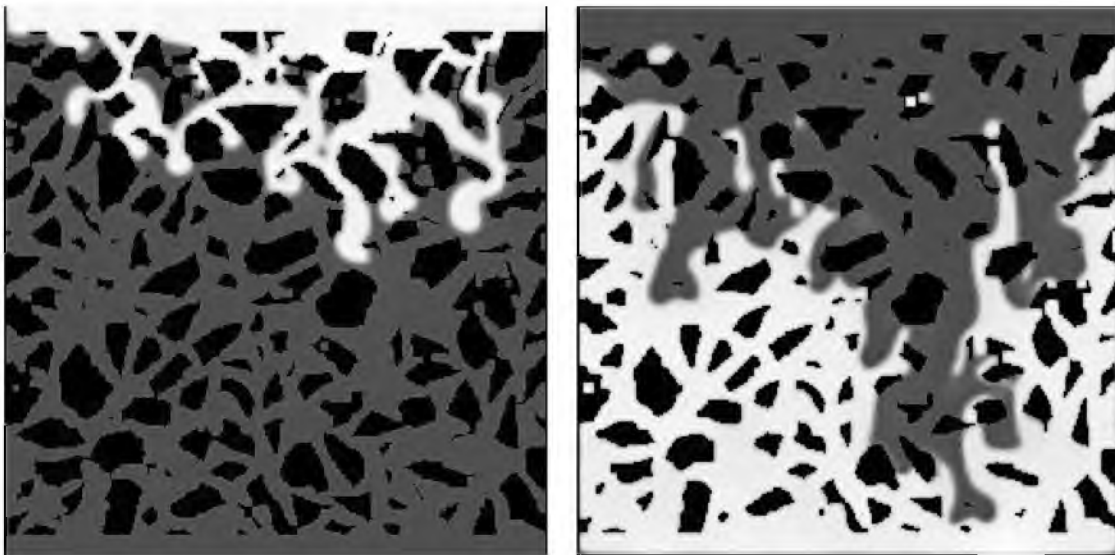
Figure 1.9: Two different simulations for the same surface tension but inverse density ratio. Left image has a density ratio = 3/1 and $Ca = 6.77 \times 10^{-2}$. Right image has a density ratio = 1/3 and $Ca = 1.32 \times 10^{-1}$. Both images were taken after 10,000 iterations.

The model is used for simulation of fluid penetration into porous samples and the analysis of capillary phenomena. The use of the LBM is not only for velocity profiles or flow simulations of single components as showed before. The LBM can also be used for multicomponent, multiphase situations. For these simulations, the LBM algorithm is changed a little and a new index relevant to the arrays of the lattice and new loops for the two components is introduced (Lin et al., 2010). The multicomponent simulations have been of great importance for industry for the past few years. They are, for example, of significant importance for the oil industry because petroleum is often found with water. Another important example is that of filtration processes in the mineral processing industry. In this case, the interaction between air and water is studied and simulated and its numbers are applied to the filtration process.

In order to gain a better understanding of the complex transport phenomena that occur in a microscopic scale, the study of the LBM is necessary. The LBM showed that it effectively integrates different equations and parameters to simulate the fluid flow in complex and regular geometries. Different examples were presented and proved to be an excellent tool for the investigation of fluid flow. The implementation of these simulations showed that changing different parameters changes the behavior of the fluid. These results are comparable to experimental data that have been already gathered. The LBM is so diverse and can be applied to different areas of research and it is, indeed, a tool that makes a lot of processes very economical since the simulation mimics the actual process. It was demonstrated that simulation results from the LBM are in good quantitative agreement with experimental results. The LBM can be considered to be an efficient numerical method for computational fluid dynamics, and a powerful tool for modeling

new physical phenomena that are not easily described by macroscopic equations (Chen, 1998).

1.3 Research Objectives

High resolution x-ray microtomography (HRXMT) has the advantages of creating more powerful venues for the 3D characterization of pore network structures in different filtration cakes. Fine coal filtration and dewatering are of great importance to the coal industry and it is important to improve our understanding of water removal from filter cakes. Using HRXMT, with a voxel resolution of less than 1 micron, particles as small as 5 microns can be distinguished and described. Moreover, it is a practical and advanced tool that would help model the pore network structure of the filter cake.

In order to gain a better understanding of the complex transport phenomena that occur in a filter cake, a comprehensive study in the effects of three-dimensional pore geometry on the effective transport properties of the filter cake is necessary. HRXMT and LBM can be used together to predict and understand water removal from the pore network structures present in coal filtration cakes. The following have been identified as the research objectives: (1) HRXMT analysis of coal, silica, and glass beads particle beds to evaluate the effects of particle properties and pore microstructure on the phenomena associated with fluid flow in coal particle beds; (2) analyze the pore microstructure to determine porosity, specific surface area, porous connectivity, shape, wettability, pore size distribution and homogeneity of the packed bed; and (3) perform fluid flow simulations using the LBM under current operative conditions practiced by industry.

Regarding particle properties, particle shape and wettability will be analyzed to determine their influence on the dewatering process. Pore network structures from images of the particle beds will play an important role in determining how macroscopic and microscopic characteristics influence water retention during filtration. In addition, the application of single component multiphase flow for LB simulation of dewatering will establish parameters and conditions that will lead to improved water removal and minimum cake moisture content.

Finally, in order to evaluate the actual potential of the LBM to simulate real multiphase problems, a comparison between experimental data and simulation results will be performed with the intent of describing conditions that will lead to improved water removal and minimum cake moisture content. Of course this is a challenging problem because of the complexity of the physical phenomena involved and the size of the computing resources required.

CHAPTER 2

VACUUM FILTRATION

As has been pointed out by Leonard and Hardinge (1991), there are several factors that affect the final moisture content of coal filter cake. Among them we have the cake thickness, pressure drop across the cake, drying time, volume of air or gas pulled through the cake per unit of time per unit area, viscosity of liquid, surface tension of liquid, filter media, size distribution of solids, permeability of cake, specific gravity of dry solids, inherent moisture of dry solids, surface properties of solids, type of filter and construction, homogeneity of cake formation, temperature of solids and gas, and interfacial tension of solids, liquids and gas. Of course, a total understanding of each factor and their relationships will enable us to define conditions for minimum cake moisture content. However, such a task is overwhelming.

Currently, the methods of analysis utilize macroscopic known variables to obtain different mathematical relationships between variables that can later be used in the dewatering decision-making process. The physical laws that govern the fluid flow through a packed bed of particles during filtration are well-known. Nonetheless, the complex geometry of the pore network structure makes it very difficult to determine the relationships between variables at the microscopic level.

There is a need for fundamental filtration research since coal filtration is of great importance to the coal industry, and residual moisture in the final product is a constant problem (Ennis et al., 1994; Tien, 2006; Wakeman & Tarleton, 2005). The classical filtration approach relates the average flow rate through the coal cake with the difference in pressure and the resistance of the medium and cake itself. But in general, there is no linear or nonlinear rule for combination of the effective physical properties from the microscopic scale, which can be used to predict the macroscopic scale properties. This means that there are no current methods used to predict the variables that would result in minimum cake moisture and volume percentage of water retained in the cake after filtration.

This lack of fundamental understanding at the microscopic level during coal filtration process limits our ability to predict and resolve common operational problems such as cake cracking, water, and moisture retention. In this regard, it is essential to introduce appropriate experimental techniques and theoretical models to describe in detail the flow, which occurs at the pore scale level through a packed bed of coal particles during filtration.

2.1 Vacuum Filtration Equipment

In order to understand how various types of filters operate, one must look at the basic functions involved. In its most simplistic form, a filter provides mechanical support for a filter septum or media, a means for discharging the solids, which collect on the surface of the septum, drainage passages for removing the filtrate and gas, which pass through the cake and septum, and a means to control the pressure differential across the

deposited cake and septum. The configuration of the filtering surface (drum, disc, horizontal) dictates the types of operations that may be utilized. The internals of a filter become a hydraulic design problem, and, generally speaking, there is sufficient flexibility to provide a wide range of hydraulic capacities.

As mentioned before, there are various types of filtration operations and equipment. There are fundamental parts of the filter operation that dictate the amount of moisture retained within the cake. Industrial filtration facilities may be characterized according to the position of the slurry (the mixture of solids and water), the filter surface, which can be top feed or bottom feed, the shape of the filter (drum, disc, horizontal belt, etc.), the means of providing the driving force (vacuum or pressure), and the primary function of the filtration step, which can vary from drying to dewatering. For the purpose of this research, a top feed, leaf test vacuum filtration procedure as practiced by FLSmidth was considered due to the operating ease for a laboratory, bench-scale, setting.

2.1.1 Leaf Test Equipment

The "typical" test leaf is a cylinder with a plane area of 0.1 ft^2 (92.9 cm^2) (Figure 2.1). There will be many times when the quantity of sample is limited. While it is best to use the 0.1 ft^2 (92.9 cm^2) area leaf discussed above in order to minimize edge effects and improve accuracy, when the sample volume is limited, it is much better to have several data points with a smaller leaf than only one or two using the larger leaf. A number of tests have been run with leaves having areas of 0.05 ft^2 (46.5 cm^2) and 0.025 ft^2 (23.2 cm^2). Data with these smaller units are reasonably accurate and can be used to scale-up to commercially sized units. For the purpose of this research, the typical plane area of 92.9

cm^2 was used.

One face of the leaf is grooved to provide large filtrate drainage passages and a support for the filter medium, which is held by a clamp. A 3/8" iron pipe size (IPS) (9.5 mm) drainage connection is provided on the other face of the leaf. The test leaf is fitted with a filter medium and a shim or dam, and the assembly clamped together as shown in Figure 2.1. The depth of the shim for bottom feed tests should be no greater than the depth of the maximum cake thickness, except where cake washing tests are to be performed. In this case, the shim depth should be 1/8" (3 mm) greater than the maximum expected cake thickness. Excessive shim depth will interfere with slurry agitation and can result in the formation of a nonhomogeneous cake.
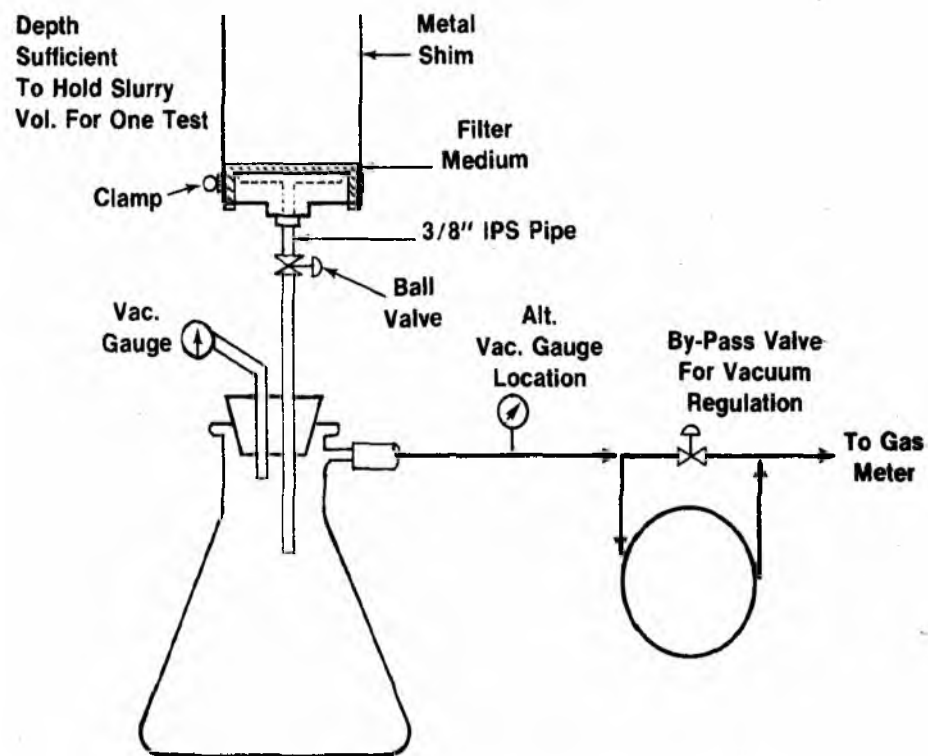
Figure 2.1: Schematic of vacuum filtration kit used to perform the filtration tests.

The back of the leaf assembly, and the joint where the shim overlaps, must be sealed with some suitable material (modeling clay for ambient or low temperature applications) so that the filtrate volume collected accurately represents the liquor associated with the deposited cake solids. Figure 2.1 also contains a schematic layout of the equipment, which is required for all leaf tests except those involving high gas flow rates. Even then, the same setup would apply, provided a vacuum pump of sufficient capacity is employed.

The shim should be held upright, as shown in Figure 2.1, and its depth should be enough to hold the slurry. A valve is desirable when running a top feed test, located between the leaf and the filtrate receiver. The test leaf is mounted on top of the vacuum receiver, depicted in Figure 2.1 by the Erlenmeyer flask. It is necessary to provide a valve between the test leaf and the receiver so that the desired operating vacuum may be obtained in the receiver before the start of a test run. It is imperative, however, that there be no restriction in this valve. The preferred choice is a ball valve with the full bore of the drainage piping. When very high airflow rates are obtained, it must be considered that the rates being measured are limited by cake resistance and not by pressure drop through the equipment.

2.1.2 Leaf Test Procedures

In the case of a top feed test, the first run is normally started with the addition of a known quantity of slurry. The results of this first run give an approximation for probable cake formation rate, cake washing rate, cake drying rate, and the type of cake discharge that must be used. It is a generally accepted to use a series of volumes that will give a

cake thicknesses of 5 to 20 mm and then to vary the dry time once an optimum cake thickness has been determined. Dry times should be over the range of 0 to 120 seconds or longer if necessary, but a zero (0) dry time should always be performed.

In any leaf test program there is always a question as to what vacuum level should be used. For materials of moderate to low porosity, a good starting vacuum level is 18 - 20 inHg, as the capacity of most vacuum pumps starts to fall off at vacuum levels higher than 20 inHg. Therefore, unless there is a critical moisture content which requires the use of higher vacuums or the deposited cake is so impervious that the air rate is extremely low, it is best to operate at a vacuum level of 20 inHg or less.

When running top feed tests, the vacuum should be applied at the same instant that the slurry reaches the surface of the filter medium. This is fairly critical when the solids involved are coarse and fast settling. However, when the feed is a thickened slurry with very little or no settling tendencies, the vacuum may be turned on at any convenient time interval after the slurry is on the filter medium.

2.2 Coal, Copper Silicate Ore, and Silica Vacuum Filtration Tests

The following section describes the different filtration tests performed for this research. Also, different materials were used to perform these tests. Laboratory work consisted primarily of determining the type of filtration tests required for the research. It was decided to perform several vacuum filtration tests with coal, copper silicate ore, and silica samples. Copper silicate ore was used for wettability comparisons due to the hydrophilic nature of the copper silicate (chrysocolla) as compared to the hydrophobic nature of the coal particles. As discussed below, copper silicate ore did not provide the

results expected; therefore, silica and glass beads were introduced into the project. The following sections describe the sample preparation and analysis methods used for the vacuum filtration tests performed during this study.

2.2.1 Particle Size Preparation

The coal sample (3 kilograms), provided by the Department of Mining and Minerals at Virginia Tech, was wet and dry screened. Since the particle size was too big for this research, a specific particle size range was deliberately selected (40 x 200 mesh size). Samples were first wet screened using a 200-mesh screen. Any particles below the 200-mesh size (less than 74 μm) were discarded from the study. The particles above 200-mesh were wet screened using screens of mesh size 140, 100, 65, 50, and 40. Any particles above the 40-mesh size (greater than 400 μm) were also discarded from the study. Once dried, the samples were dried screened, weighed, and the particle size distributions obtained. Only 500 grams were under the 40 x 200 mesh size range after screening was performed. The experimental procedure was therefore limited to the amount of sample usable for this study. The same particle size distribution and screening methods were used for all samples in this study.

For the wettability studies (hydrophobicity studies), copper silicate ore and silica samples were used. The copper silicate ore sample was obtained from the Zaldivar heap leaching operations in northern Chile, and the silica sample was purchased from U.S. Silica Company. The copper silicate ore and silica samples were screened following the same procedure as the coal sample. Copper silicate ore and silica were used due to their hydrophilic nature, thus making them good wetting indicators. Results obtained from the

filtration tests are discussed on the next sections. Tables 2.1, 2.2, and 2.3 show the calculated particle size distributions obtained after the screening of copper silicate ore, coal, and silica, respectively. Figures 2.2, 2.3, and 2.4 illustrate the particle size distributions plots obtained from the cumulative passing percentages obtained for copper silicate ore, coal, and silica, respectively.

Once the samples were screened, only the particles with size range 65x100 mesh were used for the filtration tests in order to have uniformity throughout the tests. The same amount of sample (by volume) was used for all experiments in order to have a consistent cake thickness for all tests and samples.

Table 2.1: Calculated particle size distribution for the copper silicate ore sample.

Mesh Size	Mean Mesh Size	Mean Size [microns]	Mass Retained [g]	% Retained	% Cumulative
40x50	45	354	229.88	33.29	100.00
50x65	57.5	250	248.87	36.04	66.71
65x100	82.5	177	165.02	23.90	30.67
100x140	120	125	28.13	4.07	6.78
150x200	175	88	18.68	2.70	2.70
Total			690.58		

Table 2.2: Calculated particle size distribution for the coal sample.

Mesh Size	Mean Mesh Size	Mean Size [microns]	Mass Retained [g]	% Retained	% Cumulative
40x50	45	354	173.19	33.88	100.00
50x65	57.5	250	131.8	25.79	66.12
65x100	82.5	177	83.43	16.32	40.33
100x140	120	125	70.8	13.85	24.01
150x200	175	88	51.9	10.15	10.15
Total			511.12		

Table 2.3: Calculated particle size distribution for the silica sample.

Mesh Size	Mean Mesh Size	Mean Size [microns]	Mass Retained [g]	% Retained	% Cumulative
40x50	45	354	90.4	3.31	100.00
50x65	57.5	250	862	31.56	96.69
65x100	82.5	177	927.4	33.96	65.13
100x140	120	125	632.4	23.15	31.17
150x200	175	88	219	8.02	8.02
Total			2731.2		
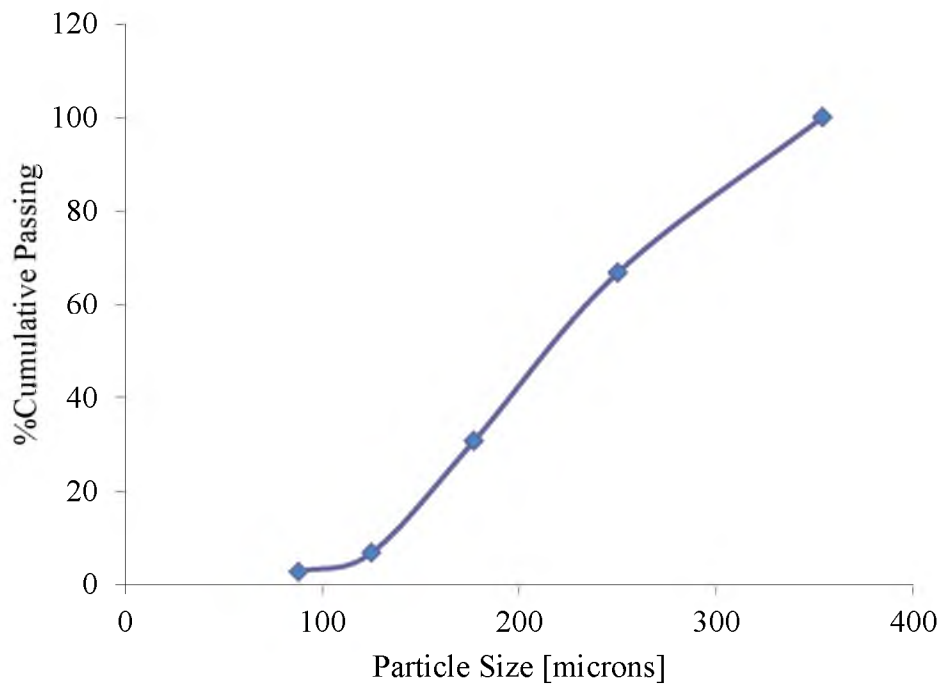
Figure 2.2: Particle size distribution plot for the copper silicate ore sample.
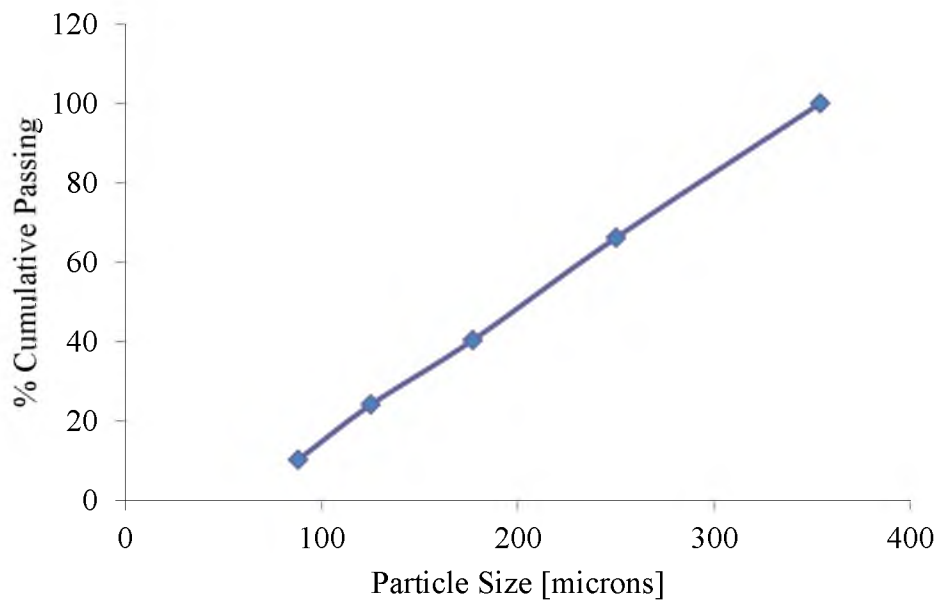
Figure 2.3: Particle size distribution plot for the coal sample.
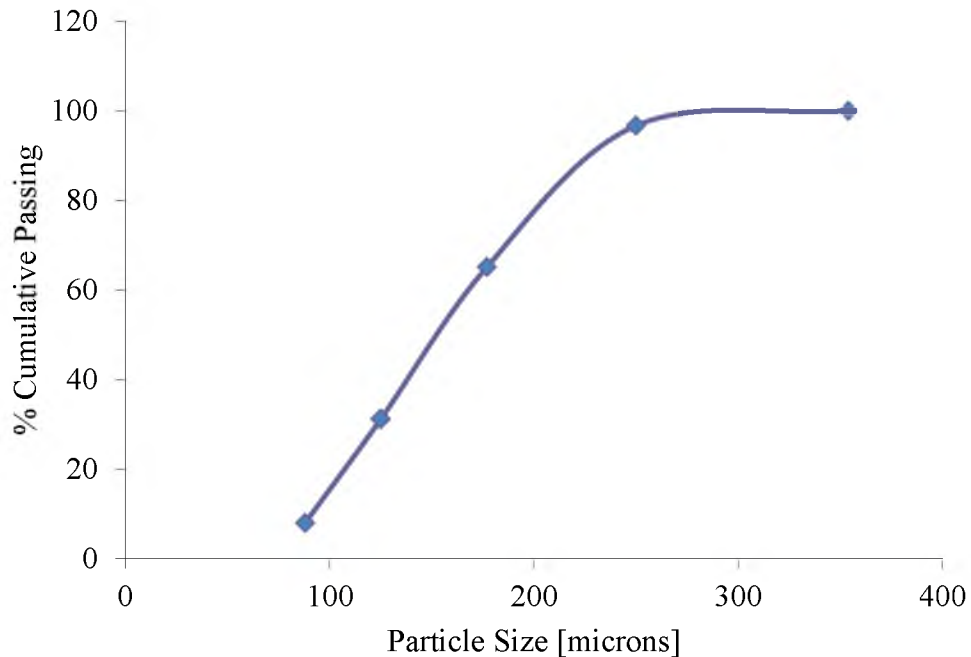
Figure 2.4: Particle size distribution plot for the silica sample.

2.2.2 Density Tests

The objective on every experiment was to generate cakes with the same cake thickness; therefore, calculations were made in order to determine how much sample was needed to obtain a consistent cake thickness. However, due to the physical characteristics of the particles involved, the density of the samples was needed in order to determine the amount of particles necessary to create filter cakes with the same volume/thickness. It was also determined that for this study every test should involve slurries containing 50% solids by weight. This means that the slurries contained a mixture of the same weight of particles and water. Nonetheless, in order to determine the weight the density for every sample was required. The density for the coal and copper silicate ore samples was measured using a pycnometer. The pycnometer is a device used to determine the density of a solid by referencing to an appropriate working fluid. In the case of solids, the net

weight of the material is measured (preparation is required in order to eliminate contaminants or vapors) and placed in a chamber in the pyctometer. The chamber is filled with a gas of known density (i.e., helium) in which the material is completely insoluble. There is a change in pressure inside the chamber caused by the presence of the sample. The difference in pressure represents the volume of the sample. The weight of the displaced fluid can be determined and hence the specific gravity of the solid. For this study, a MultiVolume Pycnometer, Model 1305, was used to determine the density of the solids. The samples were prepared and cleaned prior to measurement of density. Helium was used for this study since it is a suitable gas that penetrates the smallest pores and covers all surface irregularities. The pycnometer measured the changing pressures inside the chamber and a volume values also obtained from the machine. The data were used to determine the theoretical density of the solid.

The recorded data were used to calculate the volume of the sample first. For this calculation, the equation $V_{SAMP} = V_{CELL} - \dfrac{V_{EXP}}{P_1 / P_2 - 1}$ was used, where V_{CELL} is the empty volume of the chamber, V_{EXP} is the expansion volume, and P_1 and P_2 are the charge pressure and pressure after expansion respectively. This value was used to calculate the sample density using the equation $\rho_{SAMP} = \dfrac{W_{SAMP}}{V_{SAMP}}$, where W_{SAMP} represents the sample weight and V_{SAMP} is the sample weight. Table 2.4 shows the measured densities for the copper silicate ore and coal samples (1.25 g/cm^3 and 2.04 g/cm^3, respectively). The silica sample density was obtained from the material safety data sheet (MSDS) provided by the supplier (2.60 g/cm^3).

Table 2.4: Pycnometer data recorded and calculated density values for coal and copper silicate ore samples.

				Coal			
Weight (g)	P_1	P_2	V_{cell} (cm^3)	V_{exp} (cm^3)	V_{samp} (cm^3)	Density (g/cm^3)
0.4928	19.921	11.246	7.99654	5.86577	0.392338	1.256
0.4928	19.779	11.163	7.99654	5.86577	0.396773	1.242

			Copper Silicate Ore			
Weight (g)	P_1	P_2	V_{cell} (cm^3)	V_{exp} (cm^3)	V_{samp} (cm^3)	Density (g/cm^3)
0.473	19.819	11.290	7.99654	5.86577	0.231908	2.040
0.473	19.760	11.256	7.99654	5.86577	0.232534	2.034

2.2.3 Filtration Tests

A simple leaf test kit, as the one shown in Figure 2.1, was used to perform the vacuum filtration tests. The chosen filter media for particles ranging between 65 and 100 mesh size (149 x 250 μm) was a synthetic, polypropylene, filter cloth EIMCO POPR-859. The filtering cloth has a good tensile strength and provides a good filtering media for very small particles, such as the particle size used during these filtration tests. The pressure used for the tests was 20 inHg for every test due to the Salt Lake City altitude effect. The cake thickness for every experiment was in the range of 14 to 17 millimeters.

The procedure for each batch filtration test was as follows:

1. Agitate a known mass or volume of slurry with a mixer or by hand with a wide spatula to maintain a homogeneous suspension.

2. Transfer the slurry onto the leaf while starting the timer and simultaneously opening the ball valve.

3. Continue filtration until cake formation is complete and water disappears from the cake surface. Leave vacuum on after forming for a preselected dry time. Note whether cake cracks and the time of cracking.

4. If the cake is to be washed, pour on a measured quantity of wash water and note the time required for free water to disappear from the surface of the cake. Washing MUST begin before cake cracking occurs.

5. During each of the operations, record all pertinent information such as vacuum level, temperature, time required for the cake to crack, filtrate foaming characteristics, if any, air flow rate during the drying periods, etc.

6. At the end of the run, measure and record the filtrate volume (and weight, if appropriate), cake thickness, final cake temperature, if appropriate, wet cake weight and cake discharge characteristics (i.e., roll, sticks to media, etc.).

7. For runs involving cake dewatering only, it is usually convenient to dry the total cake sample either in an oven or under infrared lamps. A portion of the cake only may be used for moisture determination, but care must be taken to insure that a representative sample is used.

No flocculant was added to the slurry and no washing cycles were performed. Also, a back calculation of feed solids was done in order to keep track of the amount of solids in the feed slurry. The same parameters were used for every filtration test. The

drying time was the same for every test (60 seconds). Formation time was independent for every test. However, all test showed to have a formation time of 2 seconds or less. Every experiment was reproduced three times and no detrimental changes were observed regarding cake thickness, water volume percent, or cake moisture for any of the replicates. Also, the cakes revealed no cracks during the tests, thus showing that the parameters chosen were adequate. Once each test was completed, samples were taken from the cake using polypropylene straw pieces and sealed on both ends to prevent water evaporation. The samples were then scanned using the HRXMT system.

2.2.4 Test Results

The replicate filtration tests showed consistent data for the three different materials. Table 2.5 shows the results obtained from these filtration tests. The final results are highlighted indicating the vacuum formation, cake moisture, and water volume retained. The cake thickness was 14 millimeters for the copper silicate ore and for the silica cakes. The coal cake showed a cake thickness of 15 millimeters. Even though the cake thickness was similar for all tests, the cake moisture was different for all samples as well as the water volume percent. Initial results showed that the copper silicate ore sample was not a good indicator for the wettability studies. Thus, pure silica was used as a second alternative for wettability studies. The tests performed showed that cake moisture in the coal cake was much higher than the moisture content in the silica cake. The gravimetric tests indicated that the water volume retained was 31.07% and 20.49% for the coal and silica cakes, respectively.

Table 2.5: Data collected from the coal, copper silicate ore, and silica vacuum filtration tests. The initial pressure, calculated cake moisture, and water retained (vol. %) are highlighted in green.

MATERIAL   Coal, Copper Silicate Ore and Silica (149 x 250 microns)
FEED SOLIDS % (w/w)   ~50%
FILTER CLOTH   EIMCO POPR-859

TEST NO.	Coal	Copper Silicate Ore	Silica
Feed Slurry (g)	207	319	359
Form Vacuum (inHg)	20	20	20
Dry Vacuum (inHg)	15	15	15
Form Time (sec)	2	2	2
Dry Time (sec)	60	60	60
Filtrate Vol. (ml)	102	150	178
Cake Thickness (mm)	15	14	14
Cake Tare Weight (g)	4.3	4.3	4.3
Cake Total Wet Weight (g)	104.9	165.4	173
Cake Dry Weight (g)	81.4	126.48	161.7
Flocculant (g/t)	-	-	-
Net Dry Cake Weight (g)	77.1	122.2	157.4
Cake Moisture (wt. %)	23.4%	24.2%	6.7%
Back Calc Feed Solids (wt. %)	43%	45%	47%
Water weight (g)	27.8	43.2	15.6
Particle Density (g/cm^3)	1.25	2.05	2.6
Water (wt. %)	26.50	26.13	9.02
Volume solids (cm^3)	61.68	59.60	60.54
Total volume (cm^3)	89.48	102.82	76.14
Water (vol. %)	31.07	42.03	20.49

The calculations were performed in terms of water volume percentage due to the difference in density for the coal and silica particles. The results were consistent and no significant changes were observed on replicate tests. Even though lower cake moisture was expected for the coal cake, the results indicated that water retention was not only dependent on the wettability factor. The difference in cake moisture was attributed to the shape factor. The shape of the coal particles affected the cake moisture content and water percent retention because the coal particles form narrow capillaries where water is retained. It was determined that the shape of the particles plays an important role in the dewatering process. Thus, hydrophobic and hydrophilic spherical soda lime glass beads were used during the next phase of the research in order to eliminate the shape factor and complement the coal filtration results.

2.3 Glass Beads Vacuum Filtration Tests

Differences between the coal and silica particles were observed in the reconstructed 3D images obtained through the HRXMT. Coal particles showed irregular, sharp edges, while the silica particles showed more regular, smooth surface. In order to eliminate the shape factor, and complement the coal filtration results, hydrophobic and hydrophilic glass beads were used to determine the effects of particle shape in the dewatering process. With the use of spherical-shaped particles and the elimination of the shape factor, it was also easier to analyze the effect of pressure on the cake moisture. To test for the effects of pressure, the initial pressure for these tests was varied. Thus, using the hydrophilic glass beads, three different initial pressures were used. Once each test was completed, samples were taken from the cake using polypropylene straw pieces and

sealed on both ends to prevent water evaporation, and subsequently scanned using the HRXMT system.

2.3.1 Glass Beads Hydrophobization

In order to complete and complement the results for coal filtration, hydrophobic and hydrophilic spherical soda lime glass beads were also used to perform additional filtration tests. The glass beads (1200 grams) used for the tests were provided by the Department of Geology at The University of Utah. The size range of the glass beads was 200 x 240 microns. However, the glass beads were hydrophilic in nature; therefore, some of the glass beads were chemically treated to make their surface hydrophobic.

The glass beads were hydrophobized using octadecyltricholosilane (OTS), an organic molecule consisting of a long-chain alkyl group ($C_{18}H_{37}$-) with a polar head group ($SiCl_3$-). A total of 600 grams of glass beads were hydrophobized. For every 100 grams of glass beads, 500 milliliters of benzene and 2.5 grams of OTS were used. First, the benzene was poured into a beaker and OTS was added and mixed until the OTS was dissolved. Then, the glass beads were added to the mixture and placed on a magnetic stirrer. The beaker was covered to prevent solvent vaporization. It is important that the glass beads remain in suspension so that the hydrophobization becomes effective. After 24 hours, the particles were filtered, washed with chloroform, and dried at a temperature of 100°C for 4 hours. Once dried the glass beads were tested for hydrophobicity using bubble attachment time measurements. The bubble attachment tests revealed the effective hydrophobization of the glass beads and were subsequently used for the filtration tests.

2.3.2 Filtration Tests

A simple vacuum filtration kit was used to perform the filtration experiments. Figure 2.1 shows a schematic of the kit used. The same procedure used for the silica and coal samples was used for the glass beads filtration tests. The chosen filter was a synthetic, polypropylene, filter cloth EIMCO POPR-859. The pressure was varied in order to determine the pressure effect during the dewatering process. Thus, using the hydrophilic glass beads, three different initial pressures were used: 20 inHg, 17.5 inHg, and 15 inHg. For every vacuum filtration test, slurry containing 50% solids by weight was prepared. The density of the glass beads (2.60 g/cm^3) was obtained from the MSDS provided by the Department of Geology at The University of Utah. No flocculant was added to the slurry and no washing cycles were performed. The drying time was the same for every experiment (60 seconds). Once each test was completed, the same procedure used for the coal and silica samples was followed for image analysis using the HRXMT system.

2.3.2 Test Results

The filtration results for the tests performed at different initial pressures with the hydrophilic glass beads are shown on Table 2.6. Every experiment was reproduced three times and no significant changes were observed between replicates regarding cake thickness, water volume percent or cake moisture. Also, no cake cracks were observed during the tests, thus showing that the parameters chosen were adequate. Notice that as the initial pressure decreases (pressure drop decrease) the cake moisture increases, which seems to be consistent with literature (Leonard & Hardinge, 1991).

Table 2.6: Representative filtration test results and data collected from the hydrophilic glass beads tests at different pressures. The initial pressure, calculated cake moisture, and water retained (vol. %) are highlighted in green.

DATE   Feb-11
MATERIAL   Hydrophilic Glass Beads (200 x 240 microns)
FEED SOLIDS % w/w   50%
FILTER CLOTH   EIMCO POPR-859

TEST NO.	1	2	3
Feed Slurry (g)	385	387	384
Form Vacuum (inHg)	20	17.5	15
Dry Vacuum (inHg)	5	4	3
Form Time (sec)	1.5	1.5	1.5
Dry Time (sec)	60	60	60
Filtrate Vol. (ml)	194	185	190
Cake Thickness (mm)	17	17	17
Cake Tare Weight (g)	2.3	2.3	2.3
Cake Total Wet Weight (g)	190.5	190.47	192.6
Cake Dry Weight (g)	179.3	178.3	179.2
Net Dry Cake Weight (g)	177.0	176.0	176.9
Cake Moisture (wt. %)	5.9%	6.5%	7.0%
Back Calc Feed Solids (wt. %)	48%	49%	48%
Water weight (g)	13.5	14.5	15.7
Glass Beads Density (g/cm^3)	2.37	2.37	2.37
Water (wt. %)	7.09	7.60	8.14
Volume solids (cm^3)	74.70	74.26	74.65
Total volume (cm^3)	88.20	88.74	90.33
Water (vol. %)	15.31	16.32	17.36

In the case of the hydrophobic glass beads, the tests were performed with initial vacuum pressure of 20 inHg only. No tests with different initial pressures were carried out using the hydrophobic glass beads. It was observed that the cakes were not uniform such as the case for the hydrophilic glass beads. The hydrophobic glass beads agglomerated in such a way that the distribution of particles within the cake was not homogeneous. This can be attributed to the high hydrophobicity of the glass beads, which caused the particles to agglomerate or form clusters and repel the surrounding water.

In addition, the cake moisture was significantly lower than the test with hydrophilic glass beads at 20 inHg. The calculated cake moisture was 2.5%, with a water volume percentage of 8.49%, almost half the water volume percentage of the hydrophilic glass beads test at the same initial vacuum pressure. All other parameters were similar to the tests with hydrophilic glass beads at 20 inHg, as shown in Table 2.7. Thus, the results showed that when the shape factor is not a significant variable, the water retention becomes dependent of the wettability characteristics and pressure drop. As mentioned before, the shape analysis was only assessed qualitatively and not quantitatively; therefore, quantitatively analyses are required to support these data.

Table 2.7: Representative filtration test results and data collected from the hydrophobic glass beads tests. The initial pressure, calculated cake moisture, and water retained (vol. %) are highlighted in green.

DATE	Feb-11
MATERIAL	Hydrophobic Glass Beads (200 x 240 microns)
FEED SOLIDS % w/w	50%
FILTER CLOTH	EIMCO POPR-859

TEST NO.	1
Feed Slurry (g)	416
Form Vacuum (inHg)	20
Dry Vacuum (inHg)	5
Form Time (sec)	1.5
Dry Time (sec)	60
Filtrate Vol. (ml)	227
Cake Thickness (mm)	17
Cake Tare Weight (g)	2.3
Cake Total Wet Weight (g)	181.1
Cake Dry Weight (g)	176.5
Net Dry Cake Weight (g)	174.2
Cake Moisture (wt. %)	2.5%
Back Calc Feed Solids (wt. %)	43%
Water weight (g)	6.8
Glass Beads Density (g/cm^3)	2.37
Water (wt. %)	3.77
Volume solids (cm^3)	73.51
Total volume (cm^3)	80.33
Water (vol. %)	8.49

CHAPTER 3

X-RAY MICROTOMOGRAPHY

Understanding the fundamental parameters involved in the filtration process is essential in order to improve the water removal and define the condition for minimum cake moisture content. To gain better understanding of the complex transport phenomena that occur in the porous media, a study of the effect of three-dimensional pore geometry on the effective transport properties of the filter cake is necessary. X-ray microtomography was used for the characterization of the complex three-dimensional (3D) pore geometry by direct digitalization of the real pore network structure of the coal cake. High resolution x-ray microtomography (HRXMT) (Refer to Figure 1.1) allows for further advances in the 3D characterization of pore network structures in filtration cakes. With a voxel resolution of less than 1 micron, particles as small as 10 microns can be distinguished and described. The use of HRXMT and the emerging Lattice-Boltzmann Method (LBM) simulation, present a unique opportunity to explore such matters. The simulation study relied on a combination of 3D data, obtained from HRXMT measurements, and the LBM to determine the conditions to improve water removal during filtration operations.

3.1 High Resolution X-Ray Microtomography (HRXMT)

HRXMT is a noninvasive technology used to describe important characteristics of a body. In this case, HRXMT is used to effectively describe the characteristics of packed particle beds in 3D detail. This means that HRXMT has the ability to show not only the particles within the packed bed, but also the void space created by these particles known as the pore network structure. HRXMT makes use of x-rays to describe the composition of the material being studied, thus providing considerable information about the sample. In his research, Hsieh (2012) described the operational procedures for particle characterization using HRXMT.

The mechanics of x-ray tomography testing is relatively simple. The sample is located between the x-ray source and the detector (Refer to Figure 1.1). Then, the sample is irradiated with x-ray photons generated from a point source in different directions as the sample slowly rotates. As the x-rays pass through the sample, a certain amount of x-ray photons are absorbed by the sample depending on the atomic number, density, or thickness of the sample. The x-ray photons that are not absorbed by the sample are captured by the detector and a two-dimensional (2D) projection is created. These projections are created from the attenuation coefficients measured by the detector. These attenuation coefficients depend on the density and effective atomic number of that portion of the sample being examined. The attenuation coefficients determine the extent to which the material can be penetrated by the x-ray photons. Therefore, the final product will consist of several 2D images created from the x-rays passing through the sample. Finally, a computerized reconstruction is conducted. The reconstruction of the samples is based on a mathematical formalism known as the Radon transform and its mathematical

framework. After processing, the HRXMT produces a spatial description of the object under analysis where the field of view is divided into 3D elemental digital units known as voxels. Each voxel is characterized by the attenuation coefficient of the material sampled, where the attenuation coefficient can be calibrated for phase identification. This spatial digital characterization of the sample under analysis allows for further digital processing of the sample.

Figure 3.1 shows a packed bed of coal particles and its porous network structure as obtained by the micro CT system. The particle size is between 149 and 250 microns (0.149 to 0.250 mm), the resolution of each voxel is 5 μm and the size of the image is of 300 x 300 x 300 voxels. It is possible to observe how image processing of the digital data allows a clear separation between the solid particles and the air due to the clear difference in attenuation coefficients. This technique easily obtains the pore network structure of the packed particle bed.
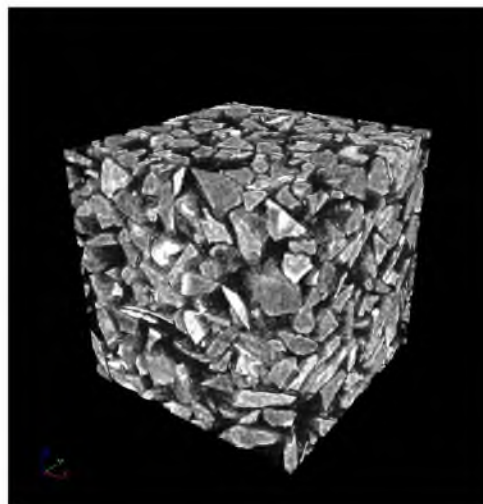
Figure 3.1: Three-dimensional (3D) image of a packed particle bed of coal with particle size of 149 x 250 μm. The voxel resolution is 5 μm and the image size is 300 x 300 x 300 voxels. The sample was scanned using 4X magnification and 40 kV.

3.2 Procedure for HRXMT Analysis

Sample analysis was carried out using a commercial HRXMT machine, the MicroXCT-400, designed by XRadia (2012). The MicroXCT-400 consists of an x-ray source, sample stage, detector, and a granite rock foundation as shown in Figure 3.2. The MicroXCT-400 features an automated system that controls the operating conditions of the machine and allows for high resolution images. The x-ray source generates x-rays that penetrate the sample and the intensity of the x-ray photons not absorbed by the sample is measured by the detector. Both the x-ray source and the detector can be positioned horizontally in order to change the field of view and the x-ray intensity. The sample stage can be adjusted vertically and has the ability to rotate the sample through a full 360 degrees. Finally, the granite rock foundation supports the x-ray source, detector, and sample stage to prevent any tilt, motion, or vibration that may affect the integrity of the image analysis during the scan.

Figure 3.2: Internal features of the XRadia MicroXCT-400.

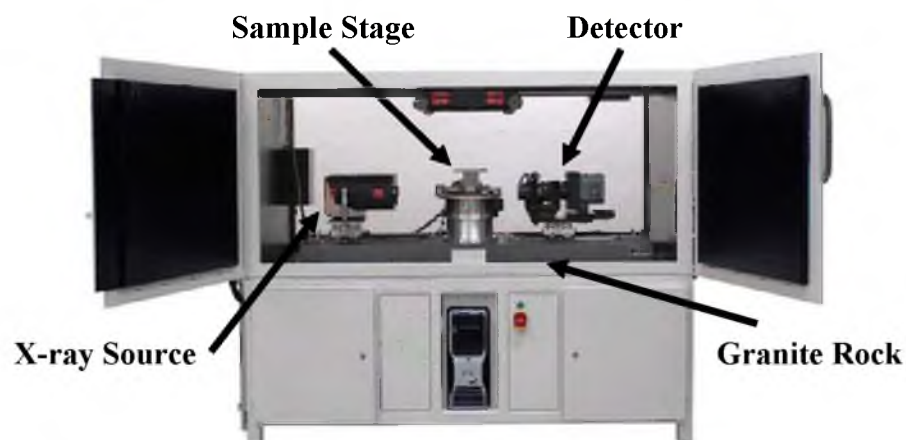The same procedure for HRXMT analysis used by Hsieh (2012) was considered for this research. According to Hsieh (2012), "the minimum particle size is required to be at least five to ten times that of the voxel resolution in order to obtain enough voxels to distinguish the particle" (p. 18). Particle size and range considerations are very important since they can affect the mass linear attenuation coefficient of the sample itself (Hsieh, 2012). Because of this, all samples were screened and a representative sample was obtained for all experiments. In this regard, the samples used for analysis satisfied the particle size and range requirements.

After filtration, samples were obtained from the filter cakes by inserting polypropylene straw pieces to the filter cake. The thin wall of the polypropylene straw pieces does not absorb a high number of x-ray photons and was used because it has a lower effect on image reconstruction. Once the sample was obtained, both ends of the polypropylene straw pieces were sealed to prevent water evaporation and to confine the particles. Scanning took place within a few hours after the samples were obtained. This method was also used to maintain the integrity of the pore network structure intact and stabilize the sample during scanning.

As indicated before, all samples were scanned under the same conditions using the MicroXCT-400. The machine requires a certain amount of "warm up" time, which usually takes approximately 15 minutes, before it is able to make its first scan. It is necessary for the machine to reach a temperature of -60°C in order for the x-ray power source and output to obtain a stable and consistent level for each scan (Hsieh, 2012). Once the machine is ready for scanning, the appropriate energy level for the source is applied. The XRadia MicroXCT-400 system is polychromatic and provides energy levels

ranging from 40 kV to 150 kV. Material properties of the samples for this research were considered in order to have an x-ray energy level that could provide high resolution images. It is important to consider the x-ray source voltage level because it also determines the attenuation coefficient (Hsieh, 2012).

Due to the low density of the samples, the coal sample was analyzed using a source voltage of 40 kV and the silica and glass beads samples were evaluated using 60 kV. The magnification for all samples was 4X and an exposure time of 9 seconds. The scan conditions for the samples were selected according to material properties and characteristics in order to obtain an accurate representation and high resolution images of the pore network structure. It is important to mention that scan conditions may vary according to material properties such as density, mineral composition, and atomic number.

3.2.1 HRXMT Image Analysis of Coal and Silica

The following sets of images represent the different 3D images obtained from the packed particle beds obtained after the filtration tests were carried out. Figure 3.3 shows a packed bed of coal particles (left) and its cross-sectional area (right) showing the void space formed after filtration, and as obtained by the HRXMT system at the University of Utah. The particle size was between 149 and 250 μm, the resolution of each voxel was 4.63 μm in length, thus providing an image size of 600 x 600 x 600 voxels. The 3D images were reconstructed using VolSuite (2009), an open source application framework used for the construction, visualization and analysis of data. The cross-sectional images

were reconstructed using ImageJ (2013), a public domain Java image-processing program.

The images in Figure 3.3 show how image processing of the digital data allows for a clear separation between the solid and the air of the pore network structure due to the distinct difference in attenuation coefficients. This technique easily obtains the porous network of the packed particle bed. During simulation the fluid flow through this network structure having a specific connectivity with well-defined pore dimensions not only to determine the local flow but also the overall permeability of the sample. The figures show how the high attenuation values (light colors) represent the high-density material and vice-versa.

Figure 3.3: Representative 3D image reconstructions of the packed bed of coal particles (149 x 250 μm) with a voxel resolution of 4.63 μm. The figure on the left shows a complete view of the HRXMT reconstructed packed bed of particles. The image on the right shows a cutoff section of the packed bed of coal particles. The image size is 600 x 600 x 600 voxels. The sample was scanned using 4X magnification and 40 kV.

Figure 3.4 shows the packed bed of silica particles (left) and its cross-sectional area (right) showing the void space formed after the filtration tests, and as obtained by the HRXMT system. The particle size and resolution of each image are the same as those of the coal images. Differences between the coal and silica particles can be observed.

Differences between the coal and silica particles were observed in the reconstructed 3D images obtained through the high resolution x-ray microtomography (HRXMT). Coal particles showed irregular, sharp edges, while the silica particles showed more regular, smooth surface. This could be a factor affecting the cake moisture content and water percent retention by the cake since the coal particles can form narrow capillaries where water is retained. Thus, hydrophobic and hydrophilic spherical soda lime glass beads were used during the next phase of the research in order to eliminate the shape factor.
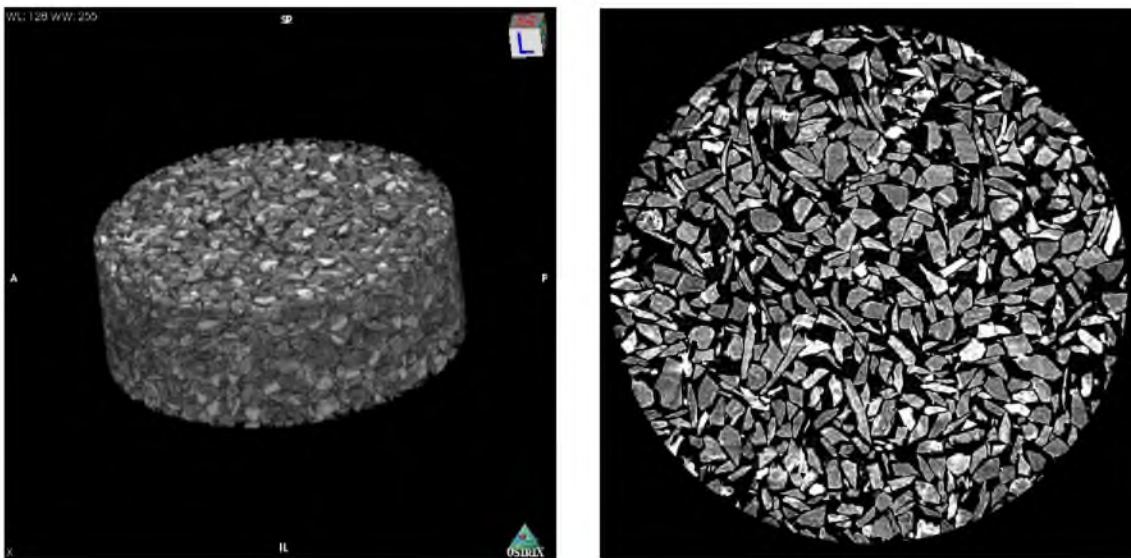

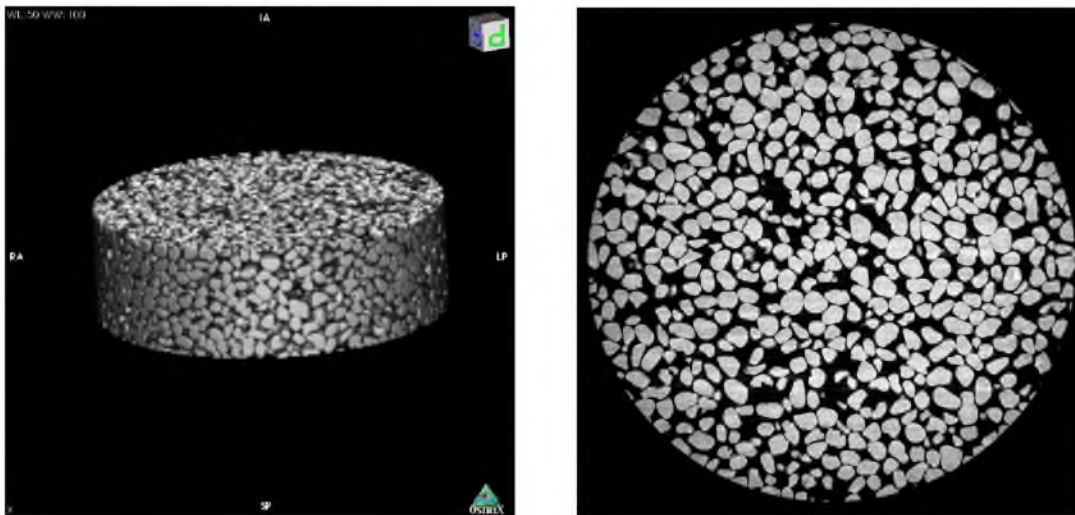**Figure 3.4:** Representative 3D image reconstructions of the packed bed of silica particles (149 x 250 μm) with a voxel resolution of 4.63 μm. The figure on the left shows a complete view of the HRXMT reconstructed packed bed of particles. The image on the right shows a cutoff section of the packed bed of silica particles. The image size is 600 x 600 x 600 voxels. The sample was scanned using 4X magnification and 40 kV.

3.2.2 HRXMT Image Analysis of Hydrophilic Glass Beads

Two different samples of hydrophilic glass beads were analyzed in order to observe the effect of the initial vacuum pressure on the amount of water retained. The two samples involved the filter cakes obtained after using an initial vacuum pressure of 15 inHg and 20 inHg, respectively. Figure 3.5 shows the representative images of the filter cakes for the hydrophilic glass beads at an initial vacuum pressure of 15 inHg. The figure shows the packed bed of hydrophilic glass beads (left) and its cross-sectional area (right) showing the void space formed after the filtration tests as obtained by the HRXMT system. The images are a reconstruction of the raw image files obtained from HRXMT. The images shown have a voxel resolution of 4.63 μm in length, and the size of each image is 600 x 600 x 600 voxels. Figure 3.6 shows a color-coded reconstructed image of the hydrophilic glass beads (green) and the water retained (red) in the filter cake formed.

Figure 3.5: Representative complete view (left) and cross-sectional (right) 3D image reconstructions of the packed bed of hydrophilic glass beads (200 x 240 μm) tested at an initial vacuum pressure of 15 inHg. The image size is 600 x 600 x 600 voxels and the voxel resolution is 4.63 μm. The sample was scanned using 4X magnification and 60 kV.

Figure 3.6: Color-coded reconstructed image of the hydrophilic glass beads filter cake obtained from the filtration tests at an initial vacuum pressure of 15 inHg. Note the water retained (red) between the hydrophilic glass beads (green) where the capillaries are formed. The cross-section was obtained from the 600 x 600 x 600 voxel 3D reconstructed image. The sample was scanned using 4X magnification, voxel resolution of 4.63 μm, and 60 kV.

Figure 3.7 shows the reconstructed images of filter cakes for the hydrophilic glass beads cake formed with initial vacuum pressure of 20 inHg. The images shown also have a voxel resolution of 4.63 μm in length and a size of 600 x 600 x 600 voxels. The image on the left shows the visualization of the filter cake and the image on the right is a cross-sectional view of the cake. From the images, it can be observed that there are no detrimental changes when compared to the images obtained from the filter cakes created at an initial vacuum pressure of 15 inHg. However, the gravimetric analysis of the cake moisture and volume percentage of water retained indicated that there were changes in the amount of retained water in the cakes. Therefore, a more thorough analysis of the capillaries and void space in the filter cakes was necessary. A detailed analysis of the medial axis calculations and the effect of capillaries formed are discussed in Chapter 4.
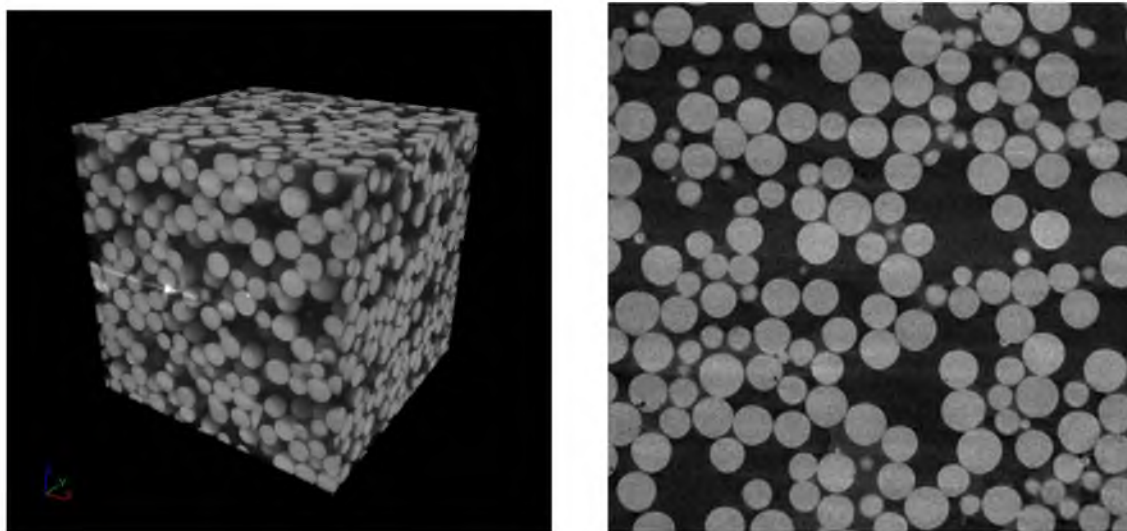
Figure 3.7: Representative complete view (left) and cross-sectional (right) 3D image reconstructions of the packed bed of hydrophilic glass beads (200 x 240 μm) tested at an initial vacuum pressure of 20 inHg. The image size is 600 x 600 x 600 voxels and the voxel resolution is 4.63 μm. The sample was scanned using 4X magnification and 60 kV.
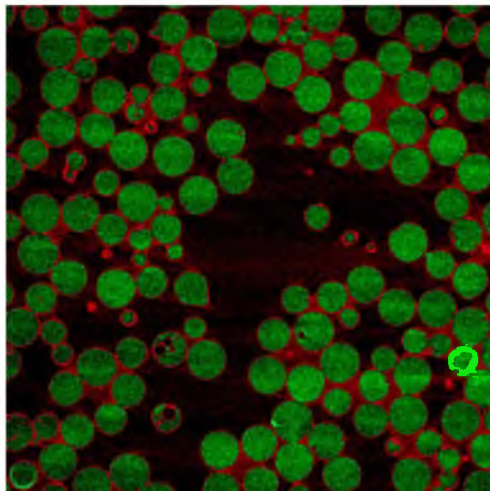
Figure 3.8 shows a color-coded reconstructed image of the hydrophilic glass beads and the water retained in the filter cake formed at an initial vacuum pressure of 20 in Hg. The red color in the cross-sectional image shows the water retained (red) between the glass beads (green) where the capillaries are formed. Figure 3.8, when compared to Figure 3.6, does not show significant changes in pore network structure. However, the calculated cake moisture and volume percentage of water retained were different. As mentioned earlier, this was attributed to the amount of capillaries formed at different initial vacuum pressures. In order to corroborate such observations, ImageJ voxel counter plugin (2010), which counts the threshold voxels in a stack and displays the volume fraction of voxels on that threshold, and medial axis analysis were performed for all tests. It was found that the percentage of small capillaries was higher at an initial vacuum pressure of 15 inHg than the number of capillaries formed in the cakes at 20 inHg.

Figure 3.8: Color-coded reconstructed image of the hydrophilic glass beads filter cake obtained from the filtration tests at an initial vacuum pressure of 20 inHg. Note the water retained (red) between the hydrophilic glass beads (green) where the capillaries are formed. The cross-section was obtained from the 600 x 600 x 600 voxel 3D reconstructed image. The sample was scanned using 4X magnification, voxel resolution of 4.63 µm, and 60 kV.

3.2.3 HRXMT Image Analysis of Hydrophobic Glass Beads

Image analysis of the filter cakes for the hydrophobic glass beads was also performed using the same procedures used to reconstruct the images for the hydrophilic glass beads cakes. Figure 3.9 shows the representative reconstructed image of the hydrophobic glass beads cake (left) and cross-sectional image (right) of the cakes. From the reconstructed image, no significant changes are visible; however, the cross-sectional image shows that clusters of glass beads were formed after filtration. When compared to Figure 3.7, the glass beads in Figure 3.9 are more dispersed and larger void spaces are formed. This is attributed to the high hydrophobization of the particles, which tends to form clusters during the dewatering process. The distance between clusters of glass beads was considerably large, thus indicating that the diameter of the capillaries for hydrophobic glass bead cakes is significantly large when compared to the hydrophilic glass bead cakes.
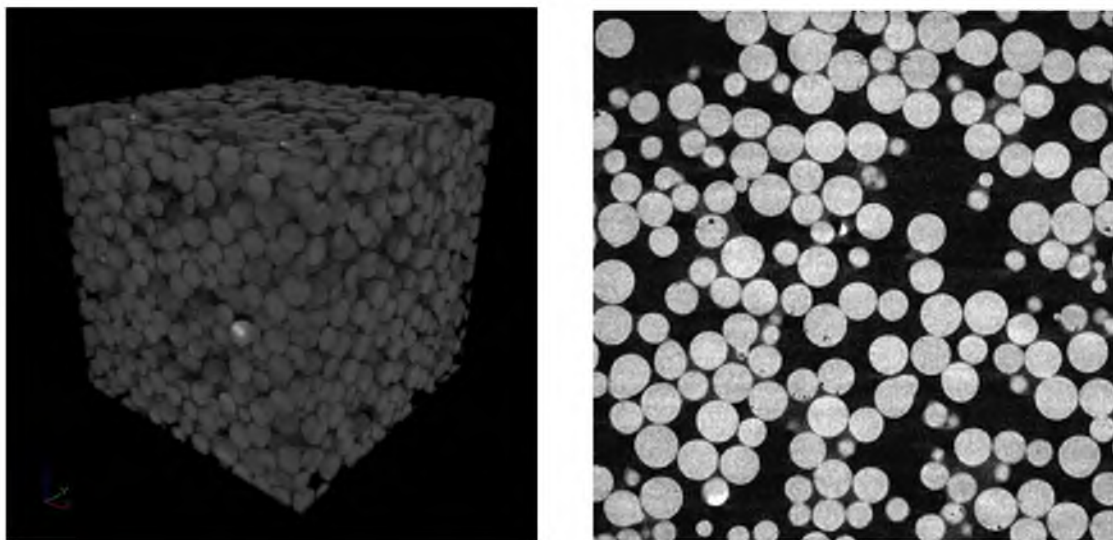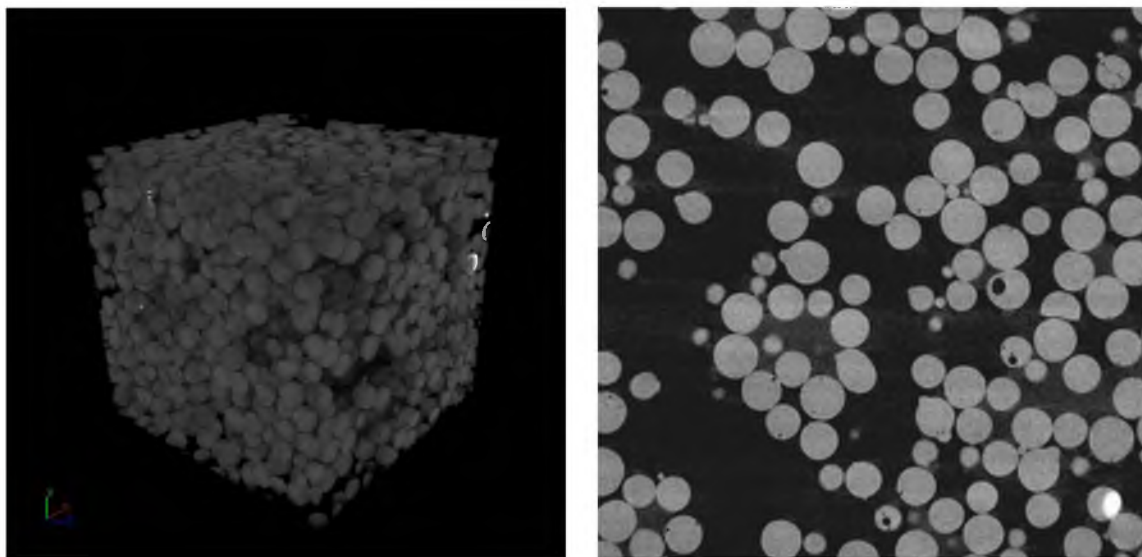
Figure 3.9: Representative complete view (left) and cross-sectional (right) 3D image reconstructions of the packed bed of hydrophobic glass beads (200 x 240 μm) tested at an initial vacuum pressure of 20 inHg. The image size is 600 x 600 x 600 voxels and the voxel resolution is 4.63 μm. The sample was scanned using 4X magnification and 60 kV.

In addition, it was observed that water was retained inside the clusters formed by the hydrophobic glass beads. Figure 3.10 shows a color-coded reconstructed image of the hydrophobic glass beads and the water retained in the filter cake formed at an initial vacuum pressure of 20 inHg. Note amount of water retained (red) between the hydrophobic glass beads (green) and the clusters formed by those glass beads. This is an indication of why, even though the glass beads are hydrophobic, the cake still has moisture of 2.5%. A gravimetric and medial axis analysis of the hydrophobic glass beads was done and it is described in Chapter 4.
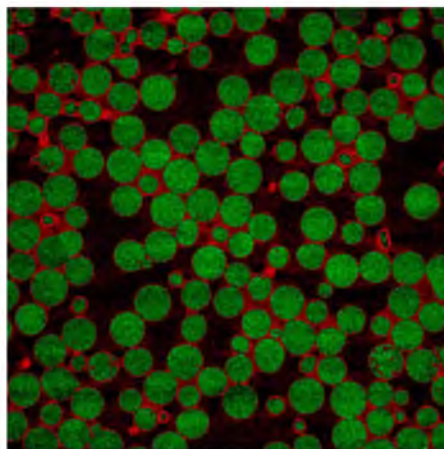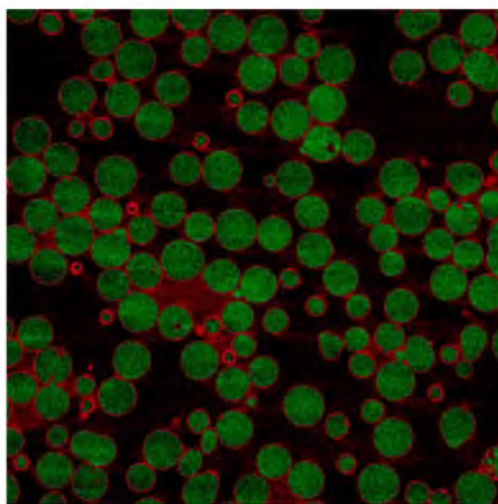
Figure 3.10: Color-coded reconstructed image of the hydrophobic glass beads filter cake obtained from the filtration tests at an initial vacuum pressure of 20 inHg. Note the water retained (red) between the hydrophobic glass beads (green) where the capillaries are formed. The cross-section was obtained from the 600 x 600 x 600 voxel 3D reconstructed image. The sample was scanned using 4X magnification, voxel resolution of 4.63 μm, and 60 kV.

CHAPTER 4

CHARACTERIZATION OF FILTER CAKE STRUCTURE

As indicated previously, the images obtained from the HRXMT were not enough to indicate the different effects of pressure or particle shape on the amount of water retained in the cakes. Therefore, an image-processing program was necessary to analyze the formation of capillaries in the pore network structure. Voxel counter (2010), a public-domain Java plug-in, was used because it determines the ratio of voxels with minimum attenuation value in a specified volume. When the attenuation values are high, the x-ray beam is highly "attenuated," or weakened, as it passes through highly dense materials. On the other hand, when the material is relatively less dense, low attenuation numbers are produced indicating that the material is practically transparent to the beam. Therefore, it is assumed that those voxels with minimum attenuation values are the voxels where capillaries are present due to the absence of highly dense particles. In addition, medial axis analysis was used to determine the number of small-diameter capillaries formed in the filter cakes. Medial axis provides the information necessary to describe the topology and geometry of a void space. In this case, medial axis was used to analyze the properties of the capillaries formed in the filter cakes.

4.1 Voxel Counter Analysis

ImageJ (2013), a public domain Java image-processing program, and the voxel counter plug-in for ImageJ (2010) were used for the voxel counter analysis of every sample. Voxel counter is a plug-in that counts the threshold voxels in a stack and displays the volume fraction of voxels on that threshold. This means that the voxel counter plug-in measures the ratio of threshold voxels (those voxels with minimum intensity or attenuation value) to all voxels. It is assumed that those voxels with minimum intensity represent the void space created in the pore network structure formed by the cake.

A predetermined threshold was set for the attenuation coefficient of the water as obtained from the HRXMT raw files. Thus, using the voxel count for the water threshold helped identify the volume percentage of water in the samples taken from each cake. Table 4.1 shows a comparison between the water volume percentage calculated from the gravimetric analysis and from ImageJ voxel counter analysis. The results show that the hydrophobic glass beads filter cake has the lowest water retention of all the samples taken into consideration. Also, it was determined that when the pressure drop is increased, the water retained in the cake decreases. Although the calculated and voxel counter quantities are not identical, the trend is the same for both analyses. This could be caused by the fact that for the voxel counter the volume considered is only a sample of the total filter cake (it is only the ratio of threshold voxels to all voxels using only a volume fraction of the reconstructed image), while the calculated values were determined using the whole filter cake.

Table 4.1: Voxel counter and calculated gravimetric results for the water volume percentage in the filter cakes.

Sample	Water Volume Percentage	
	Voxel Counter	*Gravimetric*
Hydrophilic Glass Beads (15 inHg)	12.95%	17.36%
Hydrophilic Glass Beads (20 inHg)	9.19%	15.31%
Hydrophobic Glass Beads	5.81%	8.49%
Coal	12.62%	31.07%
Silica	10.28%	20.49%

4.2 Medial Axis Analysis

A different code in C-language, called 3DMA, was used for the medial axis analysis. This code was developed by Bret Lindquist (2009) and it provides statistical analysis of the geometrical distribution of the phases in two-dimensional and three-dimensional images. Medial axis uses an algorithm to compute the skeleton of the void space. It assumes that the void space is bordered everywhere by surface grain voxels (Lindquist et al., 1996). The first step in medial axis computation is to obtain a high-resolution image regarding the spatial information of the sample indicating which voxels represent void space or dense material. The images obtained from the HRXMT created a set of voxels that defined the void-grain surfaces. These data provided the means to investigate the capillary diameter size and shape distribution of those capillaries (Lindquist et al., 1996). As a result, the pore network structure was also modeled by representing its fundamental geometry over a specified volume.

The following figures show an approximate number of capillaries according to diameter size. Figure 4.1 shows a comparison between the coal and silica samples. The percentage of small diameter capillaries (less than 46 microns in diameter) in coal is higher than that of silica. The amount of small-diameter capillaries was attributed to the irregular shape of the coal particles.

It is important to mention the significance of the formation of these small-diameter capillaries. For instance, the cake moisture volume percentage of water retained in coal was expected to be lower due to the hydrophobic nature of coal. However, gravimetric calculations performed after each filtration test showed that the water retained was higher than anticipated. Therefore, the high volume percentage of water in the cake was associated to the number of smaller-diameter capillaries. The presence of water entrapped in these small-diameter capillaries was later revealed by HRXMT image analysis and voxel counter analysis. The medial axis analysis showed that the formation of small-diameter capillaries in the coal cake had a significant effect on the amount if water retained.

On the other hand, Figure 4.2 shows a comparison between the approximate percentage of capillaries formed in the hydrophilic glass beads at an initial vacuum pressure of 20 inHg and 15 inHg. The figure shows that the number of large-diameter capillaries (larger than 46 microns) is more predominant at an initial vacuum pressure of 15 inHg. The presence of narrow capillaries in the glass beads cake filtered at an initial vacuum pressure of 20 inHg could be attributed to the pressurization of the beads. As the water is being pushed between the void spaces in the cake, the glass beads rearrange when the water is being displaced thus creating the narrow capillaries.
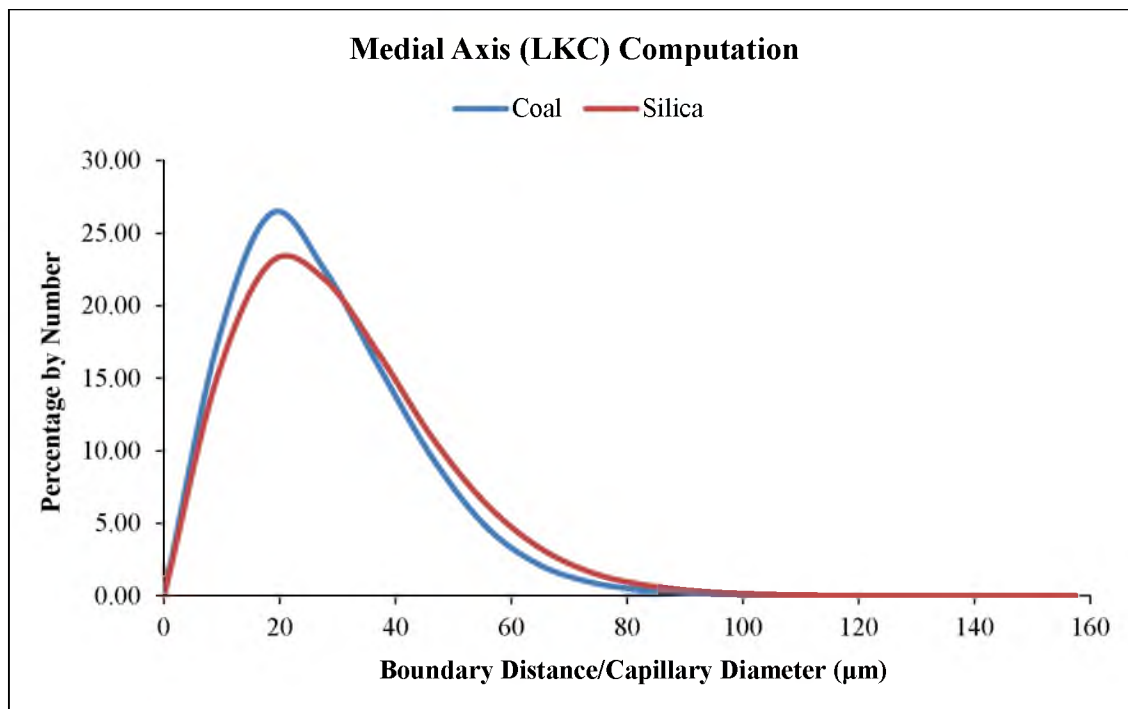
Figure 4.1: Medial axis pore analysis of the coal and silica (149 x 250 µm) filter cakes.
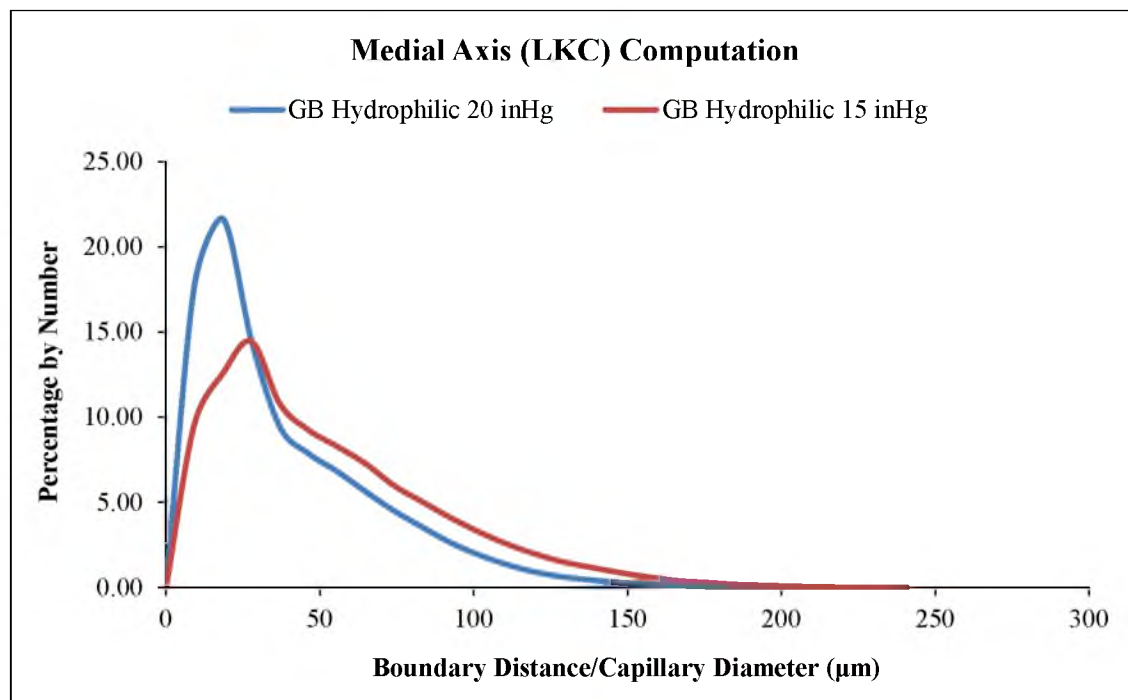

Figure 4.2: Medial axis pore analysis of the hydrophilic glass beads (200 x 240 µm) filter cakes tested at initial vacuum pressure of 20 inHg and 15 inHg, respectively.

This shows that not only wettability but also pressure changes will influence the amount of water retained in the filter cake. The presence of narrow capillaries prevents the water from filtering, but increasing the pressure drop can overcome the capillary forces and the water retention decreases. This analysis corroborates the gravimetric and image analysis results indicating that the volume percentage of water retained in the cake increases at a lower initial vacuum pressure. This demonstrates that the higher moisture retention in the hydrophilic filter cake is due not only to the size of the capillaries, but also to the change in pressure. Thus, the change in pressure affects the number of small-diameter capillaries formed within the filter cake and, therefore, the amount of water retained.

Medial axis analysis was also performed for the hydrophobic and hydrophilic glass beads samples tested at an initial vacuum pressure of 20 inHg, and the results are shown in Figure 4.3. The results showed that the hydrophobic glass beads filter cake had a higher percentage of large-diameter capillaries, and a lower percentage of small-diameter capillaries than the hydrophilic glass beads filter cake. The pore sizes for the hydrophobic glass beads ranged from 9.26 microns to 416 microns, while the hydrophilic glass beads had pore sizes ranging from 9.26 microns to 240 microns. The low cake moisture and volume percentage of water retained was attributed to the wettability factor and the amount of small-diameter pores in the filter cake. The hydrophobic glass beads filter cake repelled most of the water during the dewatering process, thus showing that the wettability plays a considerably important role in the filtration process when pressure is kept constant.

Medial Axis (LKC) Computation

——— Hydrophilic Glass Beads (20 in Hg)　　——— Hydrophobic Glass Beads (20 in Hg)
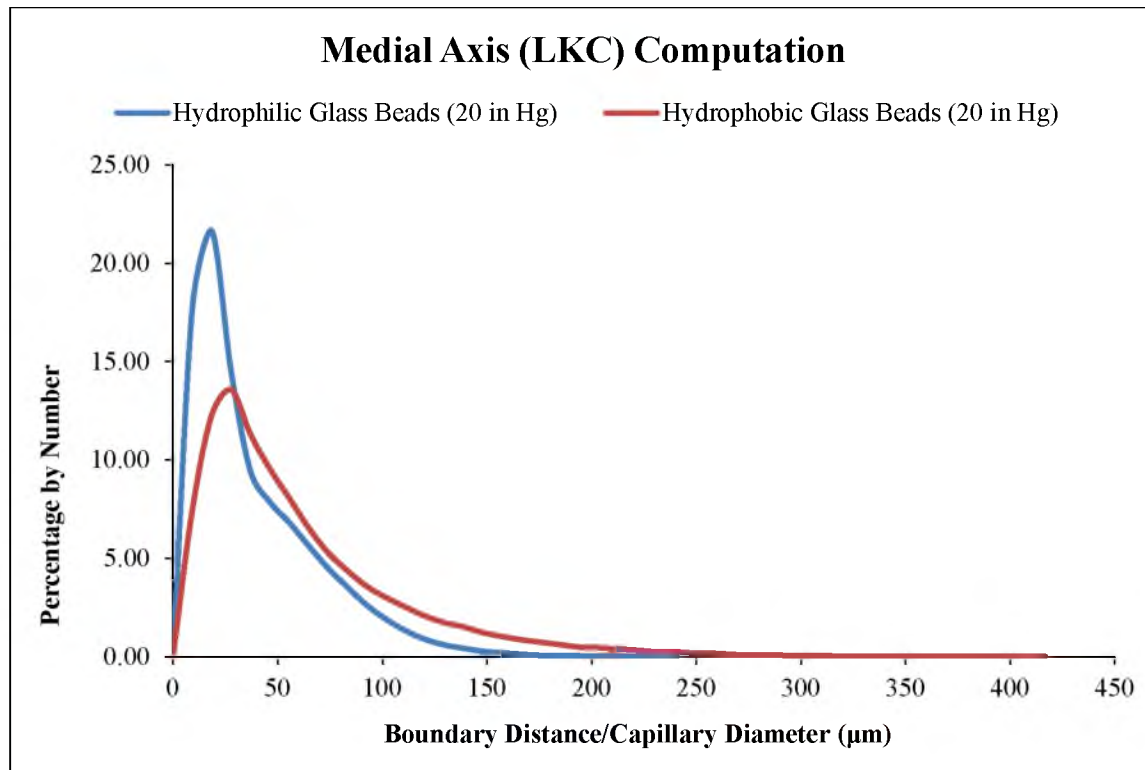
Figure 4.3: Medial axis pore analysis of the hydrophilic and hydrophobic glass beads (200 x 240 μm) filter cakes tested at initial vacuum pressure of 20 inHg.

<u>4.3 Pore Network Structures</u>

The medial axis pore computation provided the information necessary to describe topology and geometry of the void space. This topology and geometry is commonly known as the pore network structure. The pore network structure can be used to create a 3D visualization of the void space in the sample, and it can subsequently be used for Lattice-Boltzmann simulations. In this research, the pore network structure was obtained using the 3DMA code. Through a series of algorithms, the code produces a geometric analysis of the void-grain surface to describe the geometry and topography of the void space. Once this analysis is done, an image-processing program can be used to create a concrete representation of the data obtained through 3DMA.

Figure 4.4 shows the porous network structure as obtained using the 3DMA code and the image processing program VolSuite (2009) to create the visual representation of the pore network structures. All images were taken from raw image files of 300 x 300 x 300 voxels after the medial axis was computed to illustrate the difference in the pore network structures of each sample. The medial axis images have been used since they represent the skeleton of the void space. The images were color-coded to identify the diameter of the capillaries. As indicated by the caption in Figure 4.4, the red color describes 1 radius and the blue color is equal to 5 radii. Each radial unit is equal to 4.63 microns; therefore, the red and blue colors represent 9.26 microns and 46.30 microns in diameter, respectively.

It can be observed that the presence of the red colored pores in the hydrophobic glass bead filter cake is not as abundant as in the other samples. This reflects the presence of larger diameter capillaries and consequently less water retention. In the case of the silica and coal samples, the coal pore network structure had narrower capillaries than that of the silica sample, thus indicating a tendency to retain more water.

Radius Unit = 4.63 micron

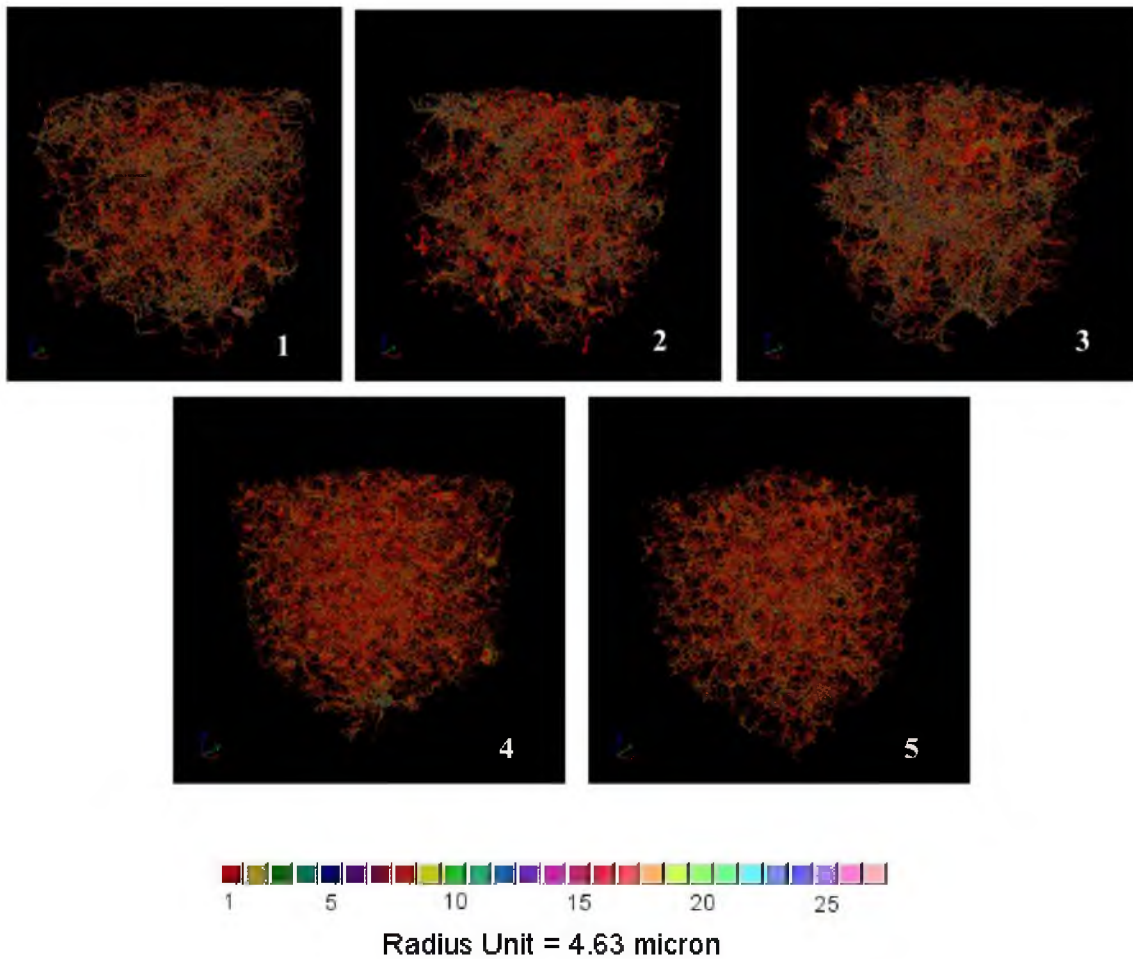**Figure 4.4:** Pore network structures of the 1) hydrophilic glass bead filter cake tested at initial vacuum pressure of 15 inHg, 2) hydrophilic glass bead filter cake tested at initial vacuum pressure of 20 inHg, 3) hydrophobic glass bead filter cake, 4) coal filter cake, and 5) silica filter cake. All images have an image size of 300 x 300 x 300 voxels.

CHAPTER 5

LATTICE-BOLTZMANN SIMULATIONS

This chapter describes the Lattice-Boltzmann Method (LBM) and presents the simulations performed during this thesis research. The LBM applies numerical simulations of fluid flow in the real porous structure which leads to the determination of the local flow conditions for single and multiphase flow in the actual complex pore structure. In this case, the intent of using the LBM is to describe the conditions that could lead to improved water removal and minimum cake moisture content during the dewatering process. The high resolution x-ray microtomography (HRXMT) results obtained from the medial axis and pore network structure analysis was used to simulate multiphase dewatering processes. However, this is a challenging problem due to the complexity of the physical phenomena involved, such as wettability and particle shape, and the size of the computing resources required.

5.1 The Lattice-Boltzmann Method Equation

The particle distribution function used in LBM was developed from the Boltzmann equation, which was formulated from kinetic theory. The particle distribution function is a function of the fluid velocity, density and temperature, and it is chosen in

such a way that its combination with a lattice with enough symmetry recovers the Navier-Stokes equation for fluid flow (Succi, 2001). It considers a gas with spherical particles moving at great velocity thus producing elastic collisions between the particles. Hypothetically, for each particle, it would be possible to know the position vector (x) and momentum (p) at some instant in time. This would give the exact dynamical state of the system and predict all future states. Thus, the system can be described as a distribution function with N number of particles, $f^{(N)}(x^N,p^N,t)$ (Sukop & Thorne, 2006). This concept also assumes that collisions are constant and no particles are lost.

The distribution function gives the probability of finding a particular particle with a given position and momentum. However, when an external force F is introduced, the position of the particle changes and it can be described by the rate of change in position and momentum at a particular time t, $f^{(1)}(x^1,p^1,t)$ *dxdp* (Sukop & Thorne, 2006). This is known as the streaming process in the model. In addition, the subsequent collision may result in some points starting at *(x,p)* arriving at the new *(x+dx,p+dp)*, while others starting at the same *(x,p)* positions will not arrive to that location. This is known as the collision process in the model (Sukop & Thorne, 2006). In order to integrate the scattered particles in the model, the terms $\Gamma^{(-)}$ *dxdpdt* and $\Gamma^{(+)}$ *dxdpdt* are integrated into the model which indicate the number of particles that do not arrive and arrive, respectively, to the expected portion of phase space due to the collisions during time *dt* (Sukop & Thorne, 2006). The expression then becomes $f^{(1)}(x^1,p^1,t)$ *dxdp* $+ [\Gamma^{(+)} - \Gamma^{(-)}]$ *dxdpdt*, which is an expression that adds the changes in the particle distribution function due to the collisions. This expression can be then expanded by Taylor series and obtain the Boltzmann equation used in the LBM: $v \cdot \nabla_x f^{(1)} + F \cdot \nabla_p f^{(1)} + \dfrac{\partial f^{(1)}}{\partial t} = \Omega$, where F is the external force,

and Ω is the collision integral ($[\Gamma^{(+)} - \Gamma^{(-)}]$). The fundamental equation for the LBM (Sukop & Thorne, 2006) is thus established. However, solving this equation analytically is very challenging and can only be done for special cases. For this, the Lattice-Boltzmann method uses relevant equations to create the simulation and solve for the equation. That means that the LBM incorporates several other equations to obtain a final solution. Hence, the LBM is not just based in one equation, but in microscopic models and mesoscopic kinetic equations. The fundamental idea of the of the LBM is to construct simplified kinetic models that incorporate the essential physics of microscopic and mesoscopic processes so that the macroscopic averaged properties obey the desired macroscopic equation (Chen, 1998).

The description of fluid motion can be done at different scales. On the other hand, the microscopic level requires the description of each fluid particle based on Newton's Law of motion and the influence of microscopic forces. This level of description has given origin to the computational branch known as Molecular Dynamics. On the other hand, we have the macroscopic level of description with computational fluid dynamics (CFD) which is based on the very well known Navier-Stokes equation and its continuum description. In between these two scales we find the LBM which belongs to the group of mesoscopic methods which are based on a statistical mechanics approximation and describes the fluid motion in terms of distribution functions.

5.2 Procedure for LBM and Multiphase Simulation Analysis

The computational procedure for the LBM simulation followed the same method indicated by Videla (2009). The samples were scanned under similar conditions and the

pore network structure was also obtained. The He-Chen-Zhang model (1999) was used to simulate the interfacial dynamics from mesoscopic kinetic equations (Videla, 2009). Simulations were carried out using representative volumes of the samples of 254 x 254 x 256 voxels in size. Even though the images obtained from the HRXMT and the image analysis software were bigger in size, the representative volume elements used for the LBM simulations were smaller due to the computer resources available. However, the scaling is representative of the whole sample and requires less computing requirements for implementation.

The implemented methods for computation (LBM) were programmed in C-language, and ParaView (2007), an open source, multiplatform data analysis and visualization application was used for 3D visualization of the simulations. The LBM was parallelized in order to reduce the processing time. Parallelization involves the simultaneous computation of different calculations that are solved concurrently. Through this process the computation times are reduced significantly. In this process, the LBM simulation was carried out using a computer with Intel Xeon dual processors, quad core machine with 2.66 GHz in each processor and a total of 64 GB in RAM memory. Each simulation was run using different iterations. It was observed during the simulations that on samples of 254 x 254 x 256 voxels in size or smaller, parallelization running in 4 processors, and for 10,000 iterations, it took approximately 20 hours to complete the simulation.

The geometry of the pore network structure obtained from the raw data using the C-language program 3DMA was programmed into the LBM code. Different simulations conditions were established before the simulation was run such as the number of

iterations, the lattice dimensions, and the boundary conditions (Videla, 2009). For each simulation, the execution time was recorded as well as the number of iterations reached for breakthrough, and an animation was generated for further image analysis. Once the simulation was completed, raw data were converted to a form that is viewable and understandable using ParaView. Visualization with Paraview allowed for a well-defined representation of the simulation in 3D space. The following section describes the analysis performed using LBM and Paraview.

5.3 LBM and Multiphase Simulations

The use of the LBM is not only for velocity profiles or flow simulations of single components as showed before. The LBM can also be used for multicomponent, multi-phase, situations. For these simulations, the LBM algorithm is changed a little and a new index relevant to the arrays of the lattice and new loops for the two components is introduced (Succi, 2001; Sukop & Thorne, 2006). In multicomponent simulation, the phase separation can be thought of as a hydrophobic interaction (Sukop & Thorne, 2006). During simulation, the fluid flows through the pore network structure having a specific connectivity with well defined pore dimensions. The simulation not only determines the local flow patterns but also the overall permeability of the sample.

The multicomponent simulations have been of great importance for industry for the past few years. They are, for example, of significant importance for the oil industry because petroleum is often found with water. Another important example is that of filtration processes in the mineral processing industry. In this case, the interaction between air and water is studied and simulated and its numbers are applied to the filtration process.

The He-Chen-Zhang model (1999) and the images obtained from the HRXMT analysis were used to simulate flow in each filtration cake studied. The HRXMT images provided a digital representation of the pore network structure showing the complex geometry of the capillaries. On the other hand, the He-Chen-Zhang model (1999) provides the means for single component multiphase flow using the LBM. It is important to mention that, although the images analyzed during this research were of sizes 600 x 600 x 600 voxels, the processing and computer capabilities were not sufficient to evaluate and simulate fluid flow on those images. Therefore, the images were reduced to a smaller size.

Figure 5.1 shows the reconstructed coal and silica images obtained from the HRXMT. The particle size range is 149 x 250 μm and the subset images are 254 x 254 x 236 voxels. It is important to indicate that the subset size is significantly small because the computational capabilities to run the LBM were limited. The medial axis and voxel counter analysis were also generated and calculated to carry out the LBM simulations.

The results from the LBM simulations run for the coal and silica filter cakes are shown in Figures 5.2 and 5.3, respectively. Again, due to the computational capabilities at the University of Utah, only a few iterations were run. This is a time-consuming process and saturating the computer with a large number of iterations may crash the program. It is noted that the penetration of the fluid front for silica with 30,000 iterations is almost the same as the penetration of the fluid front for coal with 60,000 iterations.
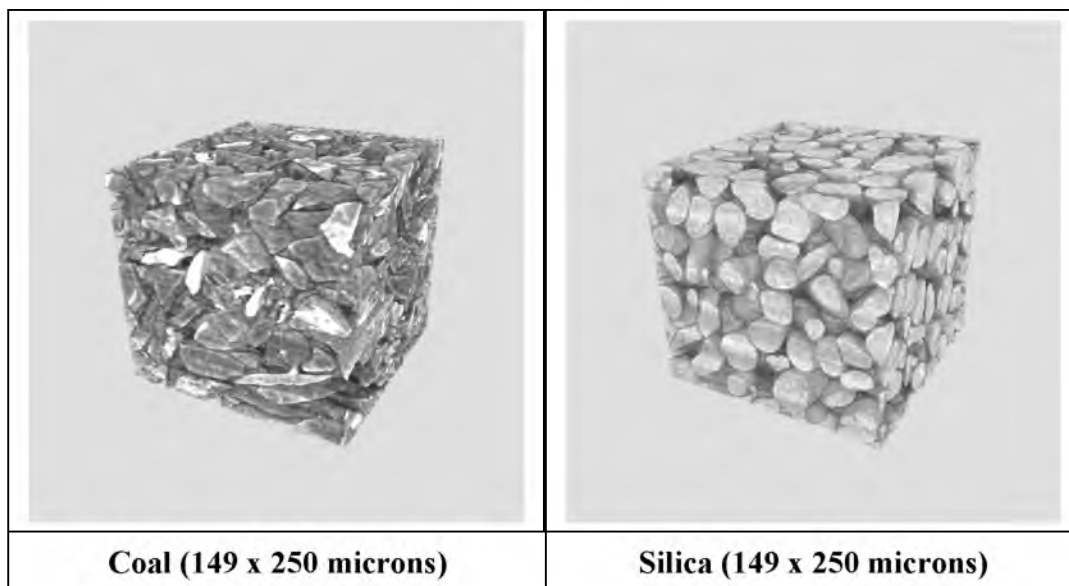
Figure 5.1: Subset of the 3D image reconstructions of the coal and silica filter cakes with particle sizes of 149 x 250 microns and a voxel resolution of 4.63 μm used for 3D LBM simulations. The image size is 254 x 254 x 236 voxels. The coal sample was scanned using 4X magnification and 40 kV. The silica sample was scanned using 4X magnification and 60 kV.

Figure 5.2: Results of LBM simulations of multiphase flow through a packed bed of coal filter cakes with particle size of 149 x 250 µm and image size of 254 x 254 x 236 voxels. Images show fluid penetration after 60,000 iterations.
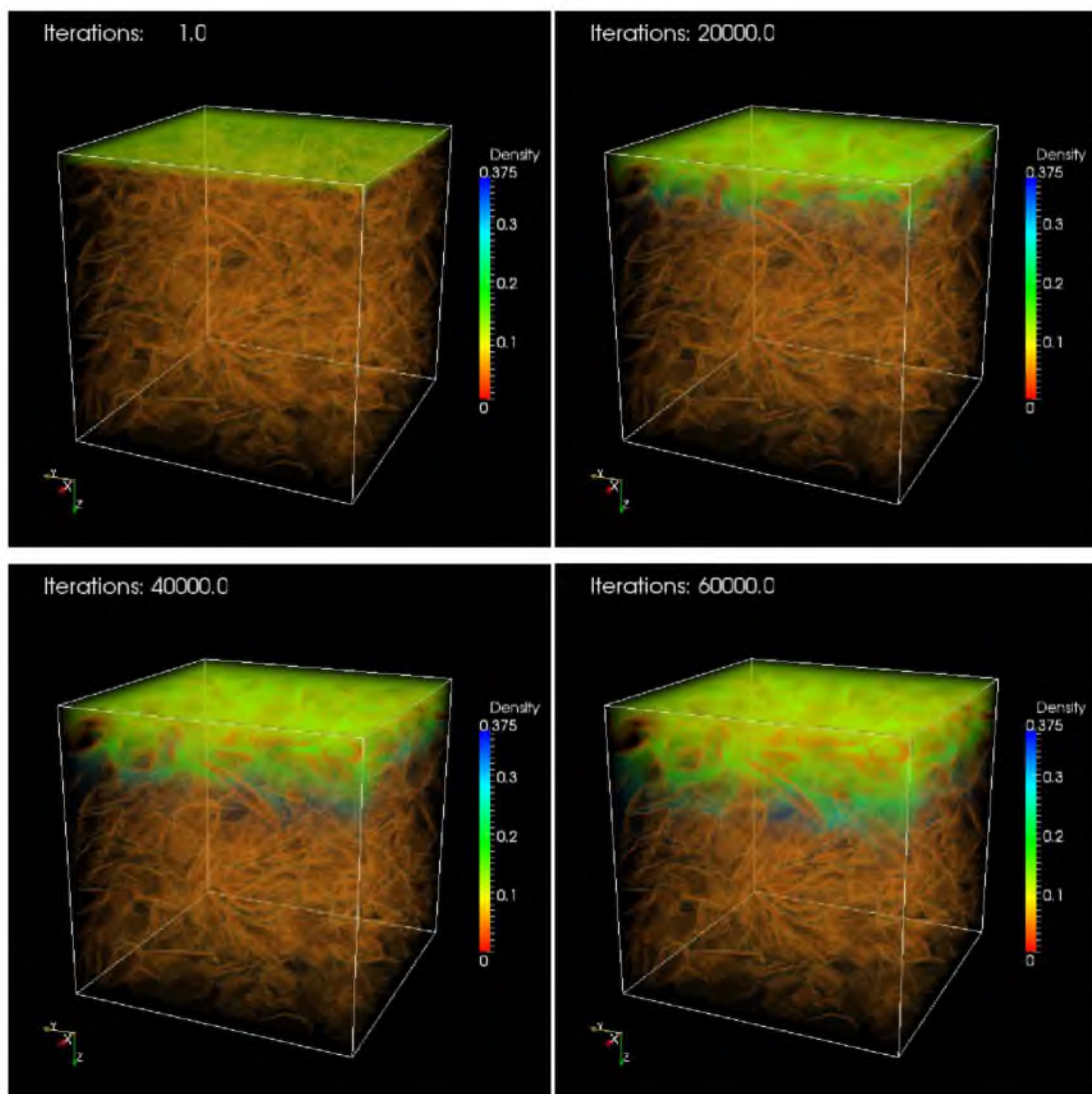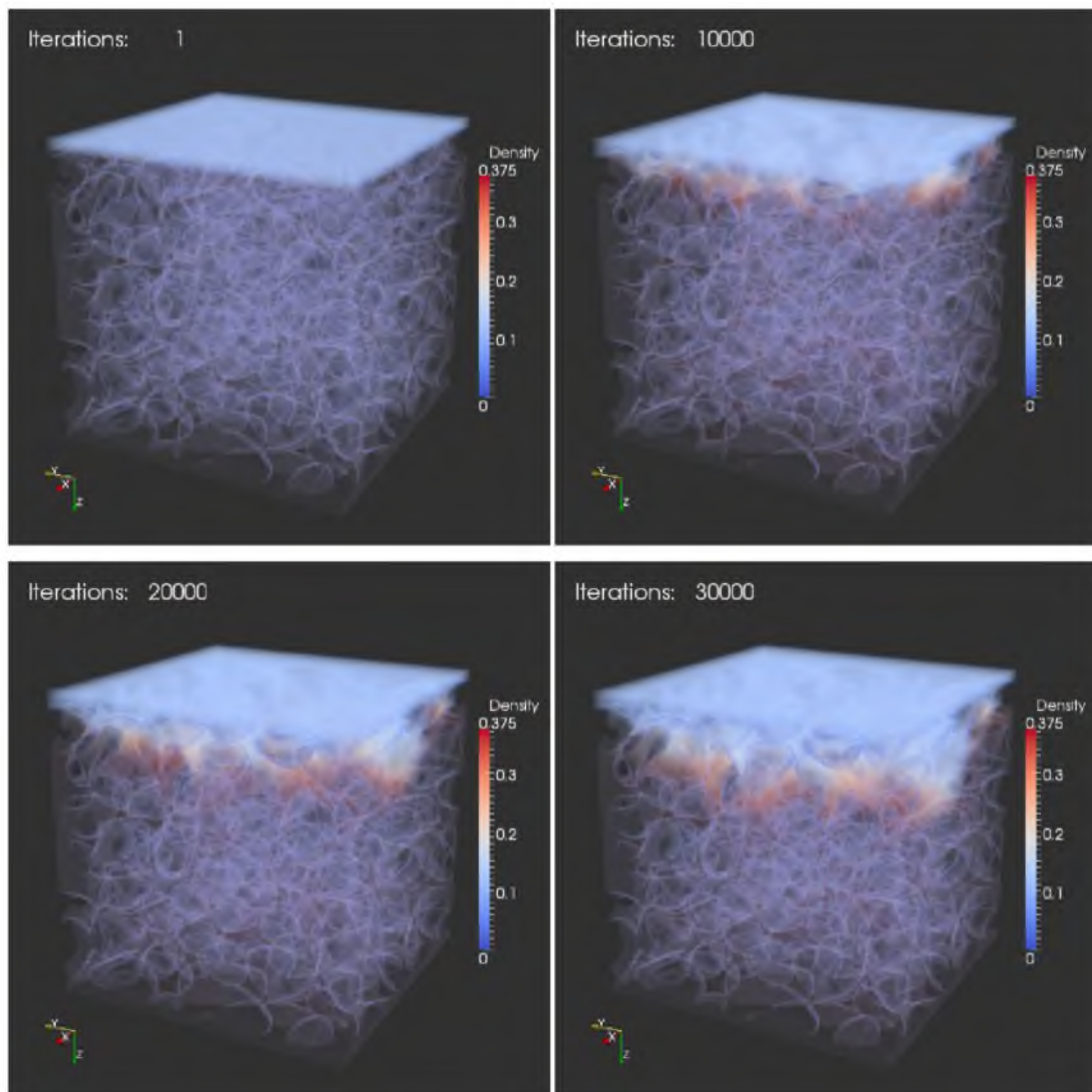
Figure 5.3: Results of LBM simulations of multiphase flow through a packed bed of silica filter cakes with particle size of 149 x 250 μm and image size of 254 x 254 x 236 voxels. Images show fluid penetration after 30,000 iterations.

It can be observed in Figures 5.2 and 5.3 that the fluid does not go through completely from the top to the bottom of the filter cake subset. Evaluating the actual potential of the LBM to simulate real multiphase problems was challenging not only because of the complexity of the physical phenomena, but also because of the size of the computing resources required to run simulations for larger subsets.

Each simulation required an intensive use of computing resources. Running simulations on large subsets is not very practical since the memory requirements are extremely large and the processing times are very long. Because of this, sometimes it is convenient to parallelize the LBM. Through parallelization, many calculations can be carried out simultaneously and concurrently using multiple processors. This accelerates the LBM computations and the results are available faster. For this research, the single component multiphase He-Chen-Zhang model used for the LBM simulations was parallelized. The simulations were performed using a computer with Intel Xeon dual processors, quad core machine with 2.66 GHz in each processor, and a total of 64 GB in RAM memory. A typical simulation for a 256 x 256 x 256 lattice for 10,000 iterations took approximately 20 hours (parallelization running in 4 processors), and used around 12 GB in RAM memory or 715 bytes/node. Depending on the sample, approximately 100,000 to 200,000 iterations were required for the breakthrough of the whole packed particle bed (256 layers). Now, graphics processing units (GPU) accelerate and facilitate the computations for these simulations. GPU computing is continually evolving and the processing time for this type of analysis is expected to be reduced.

In this regard, breakthrough for the filter cake is the parameter that indicates when to terminate the simulation and determine the residual moisture content inside the filter

cake. The breakthrough for the coal sample required more iterations than that of the silica sample. Figure 5.4 and Figure 5.5 show the simulated penetration of the fluid front for coal and silica at different iterations, respectively. The images on the left show the fluid flow penetration, while the images on the right show the fluid retained in the sample. It can be observed that at breakthrough points the fluid is completely displaced using the simulations and image reconstructions. Figure 5.3 also shows the formation of finger-like capillaries growing in all directions. These capillaries trap the displaced fluid and lead to a higher moisture content in the sample. This is representative of capillary fingering described by Lenormand et al. (1988) and Lin et al. (2010), and becomes the dominant force in the dewatering process. On the other hand, the silica sample (Figure 5.4) exhibits continuous finger-like that spread across the porous network. In this case, the major force is due to capillary fingering but with relatively short fingers.

Figure 5.4: Surface of the penetration of fluid front is extracted at 80,000 iterations during LB simulation for coal filter cake with particle size 149 x 250 μm and image size of 254 x 254 x 236 voxels. The image on the left shows the fluid penetration and corresponding breakthrough. The image on the right shows the fluid retained in the sample after 80,000 iterations.
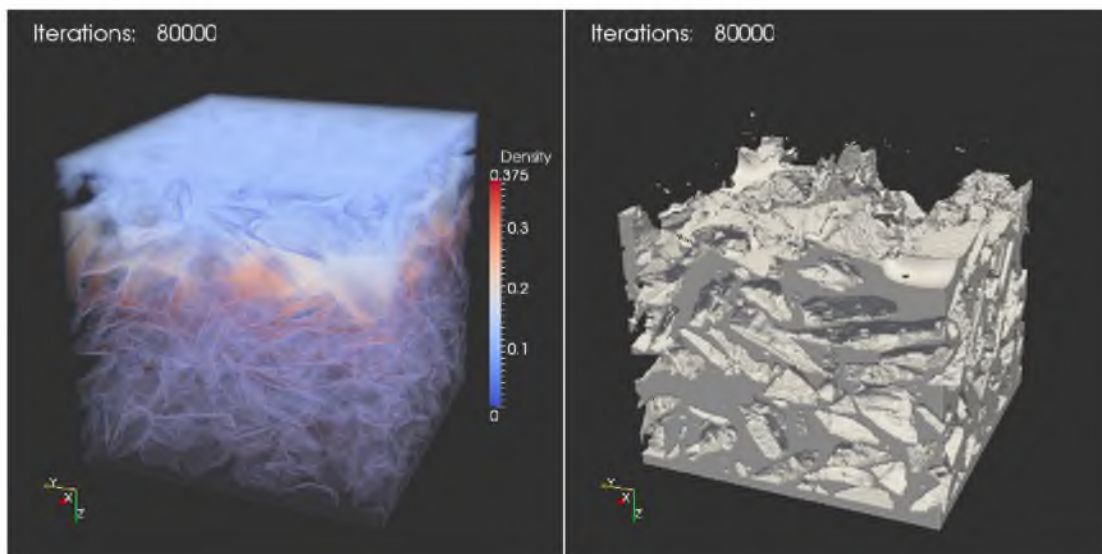
Figure 5.5: Surface of the penetration of fluid front is extracted at 40,000 iterations during LB simulation for silica filter cake with particle size 149 x 250 μm and image size of 254 x 254 x 236 voxels. The image on the left shows the fluid penetration and corresponding breakthrough. The image on the right shows the fluid retained in the sample after 40,000 iterations.
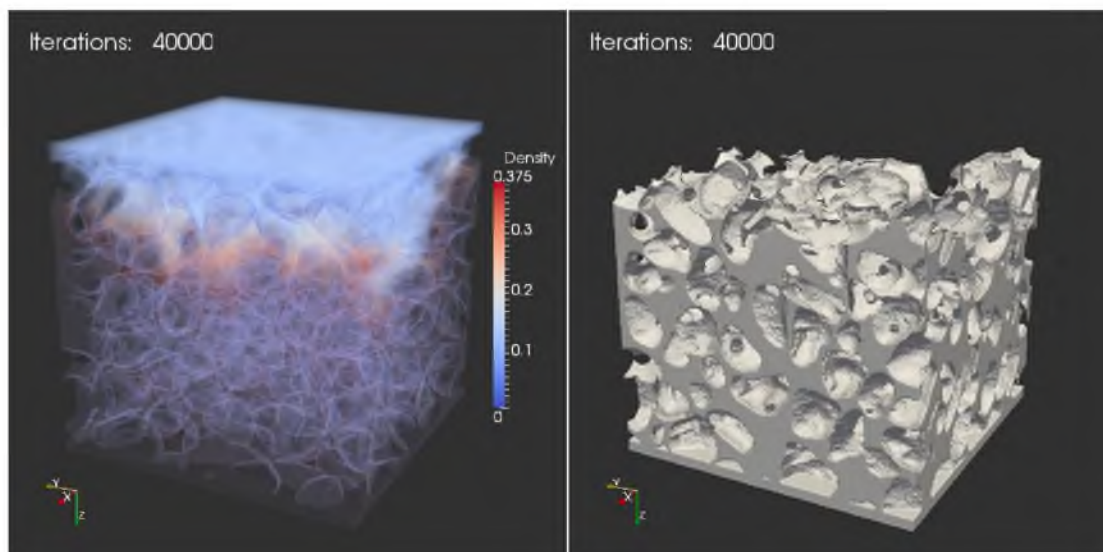
Figure 5.6 shows 3D simulations of the fluid front penetration using the He-Chen-Zhang model applied to a packed bed of hydrophilic glass beads using the reconstructed pore network structure from the HRXMT image analysis. In this simulation, the fluid penetration was induced by a fixed pressure difference using the LBM. The same procedure used to analyze the fluid penetration for coal and silica was used for this sample. The density parameter was also established for this simulation so that the low-density fluid displaces the heavy fluid (density ratio 1 to 3). According to the Lenormand diagram (Figure 1.6) a stronger viscous fingering type of flow was expected as more and longer fingers were formed due to the stronger viscous interaction and interface front instability. As the comparison shows, there is a clear qualitative agreement between theory and simulations. Fingers are formed in zones of low resistance to flow and once
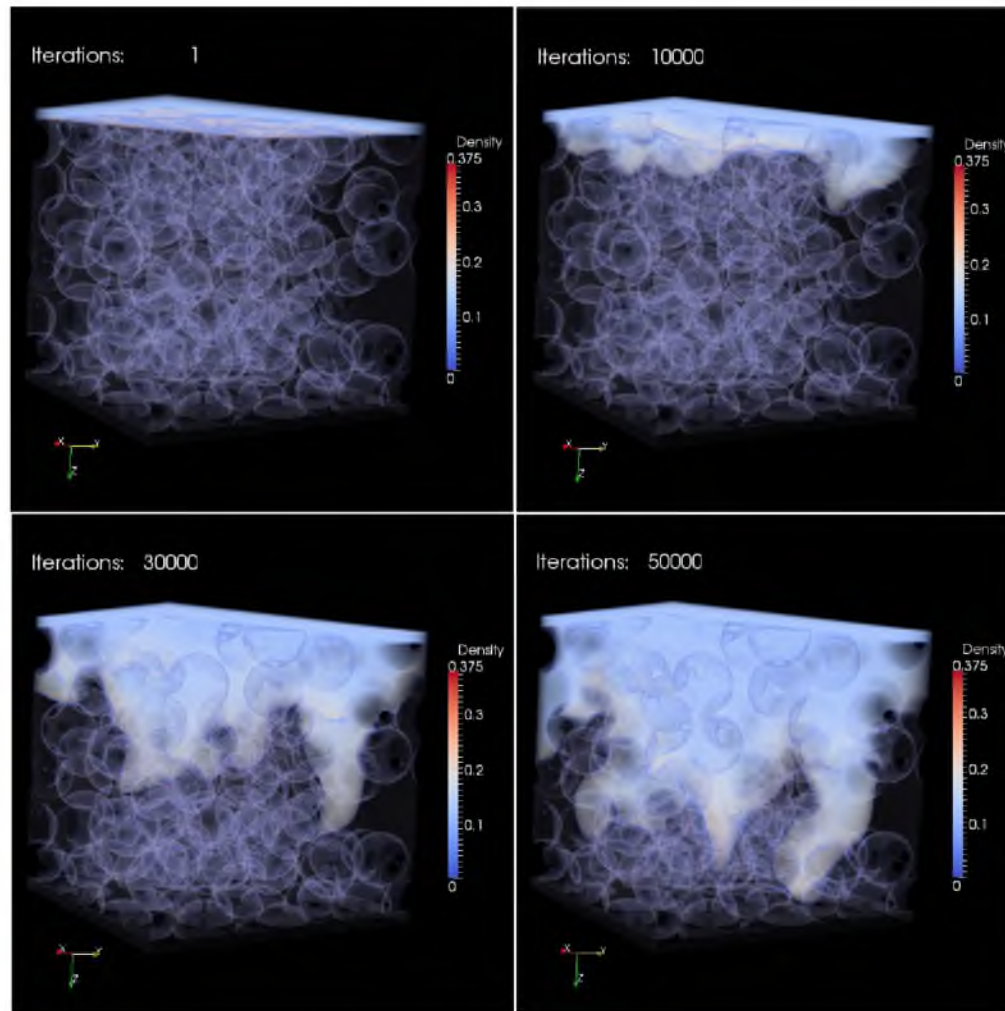
Figure 5.6: Sequence of simulations of two-phase flow in a packed bed of hydrophilic glass beads particles (200 x 240 μm). Percolation simulations by the single component He-Chan-Zhang LBM. (Density ratio = 1/3; Lattice size of 256 x 256 x 256 voxels; Images for 1, 10,000, 30,000 and 50,000 iterations).

formed they start growing rapidly towards the exit. In fact, the lower images (at iterations of 30,000 and 50,000), 5 to 6 fingers are clearly identified (lower right-side image). The breakthrough for the filter cake, which depends on the deepest finger tip, is the parameter to terminate the simulation and determine the residual moisture content inside the filter cake. In this case the breakthrough value was 50,000 iterations.

Figure 5.7 shows the comparison of the same 3D simulations of the interface advance shown in Figure 5.6 against a new simulation where packed silica sand (149 x 250 μm) was used. It can be observed in Figure 5.7 that the simulation starts from complete saturation (one iteration) and continues to displace the fluid as the number of iterations is increased. The low-density phase displaces the high-density phase until it reaches the breakthrough point after 120,000 iterations. As the high-density phase is being displaced, the low-density phase moves through paths of least resistance (coarse pore diameters). However, the low-density phase is not able to penetrate and move through small pores due to the high flow resistance. Therefore, some residual high-density phase gets trapped in the small-diameter pores. The presence of narrow pores prevents the high-density phase from moving, and only an increase in pressure drop can increase the flow of the high-density phase through these narrow pores. According to the Lenormand diagram (Figure 1.6), the pattern of percolation shows a capillary fingering type of flow with relatively short fingers. It was noted that the penetration of the fluid front for complete breakthrough for packed beds of silica sand and hydrophilic glass beads were 120,000 and 50,000 iterations, respectively.
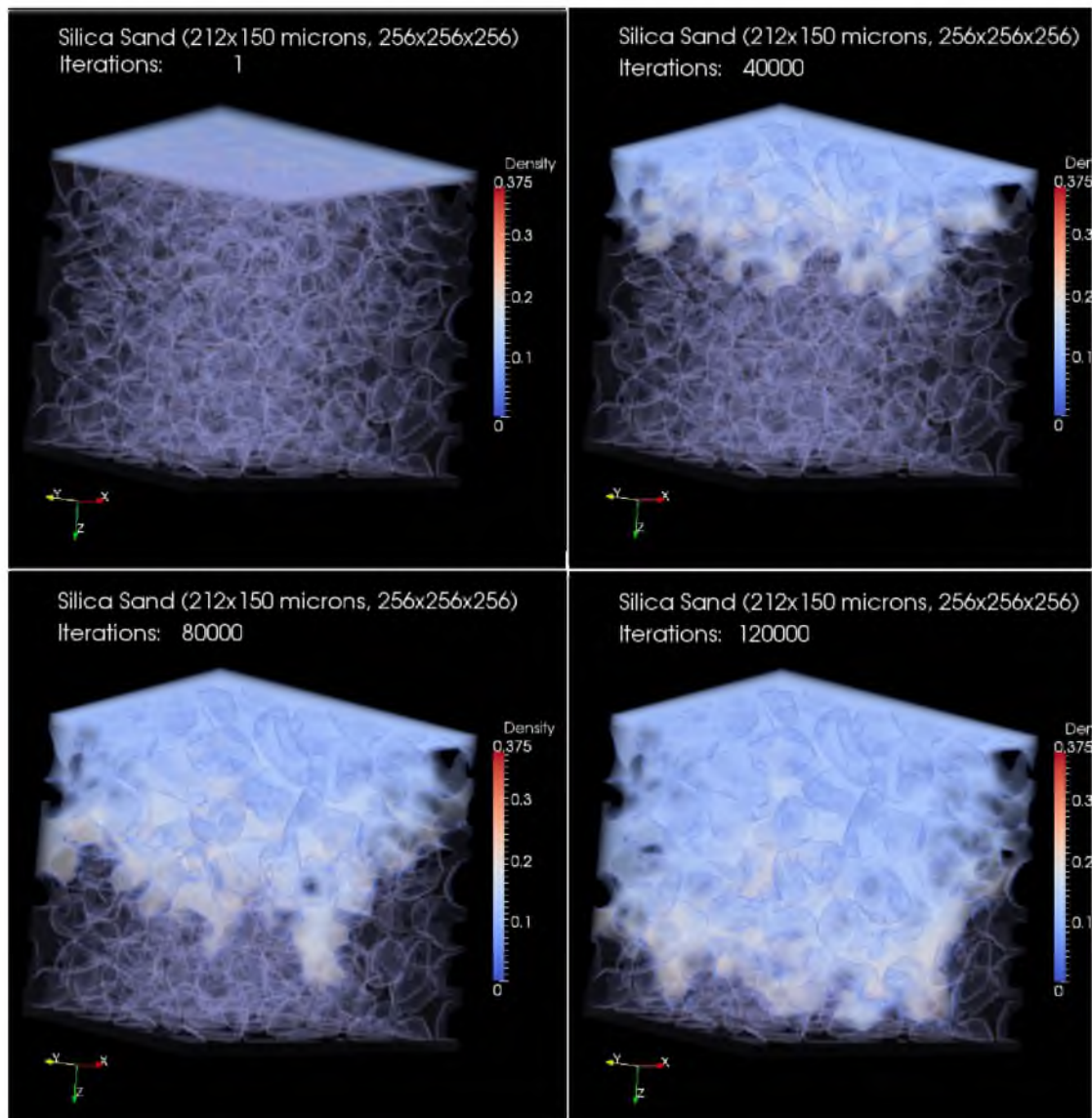
Figure 5.7: Sequence of simulations of two-phase flow in a packed bed of silica sand particles (particle size 150 x 212 μm). Percolation simulations by the single component He-Chan-Zhang LBM. (Density ratio = 1/3; Lattice size of 256 x 256 x 256 voxels; Images in increments of 40,000 iteration steps each).

CHAPTER 6

CONCLUSION

The combination of HRXMT image analysis and LBM simulations demonstrated the actual potential to simulate real multiphase problems. The analysis obtained from the simulation results can be compared to experimental data in order to describe the conditions that can lead to improved water removal and minimum cake moisture content during the dewatering process. Moreover, the characterization obtained through HRXMT, with resolution of less than 1 micron, can be used to analyze particles as small as 10 microns. This becomes important especially when very small particles are present in filter cakes.

The analysis performed on coal and silica filter cakes showed that particle shape is one of the most important factors in the retention of moisture during filtration when other characteristics are kept constant, as shown in Chapters 4 and 5. Because of this, spherical glass beads were used to eliminate the effect of particle shape. In addition, to incorporate the wettability effect, half of the glass beads were hydrophobized with OTS. As expected, the vacuum filtration tests (Tables 2.6 and 2.7) showed that, in fact, hydrophobic particles retain less moisture than the corresponding hydrophilic particles.

In addition, it was observed that the hydrophobic glass beads agglomerated in such a way that clusters were created trapping water after filtration (Figures 3.9 and 3.10). This was attributed to the high hydrophobicity of the glass beads. The results showed that when the shape factor is not a significant variable, the water retention becomes dependent on the wettability characteristics and pressure drop. The wettability effect of the particles studied in this research is consistent with other studies regarding wettability effects in the dewatering process (Asmatulu & Yoon, 2012; Yoon et al., 2006).

Moreover, tests with different pressure drops were performed for the hydrophilic glass beads. Although the pore network structure analysis showed that the capillaries were narrower at higher initial vacuum pressures (Figure 4.2), the increase in pressure drop decreased the amount of water retained in the filter cake. This was corroborated through gravimetric calculations and voxel counter computations (Table 4.1) that showed the same trend indicating that the volume percentage of water retained in the cake increases at a lower initial vacuum pressure. The pressure drop increase helped overcome the capillary forces that retain the water in the filter cakes.

The HRXMT images were reconstructed using ImageJ in order to visualize the overall 3D image. Also, the 3DMA code and the open source software VolSuite, ImageJ, and ParaView were used to reconstruct the pore network structure (Figure 4.4). The processing programs showed that the pore network structure has a big influence on the retention of water in the filter cake. After voxel counter and medial axis analysis, narrow capillaries were found in the filter cakes with hydrophilic particles, while wider capillaries were mostly found in the filter cakes with hydrophobic particles (Figure 4.3).

The hydrophobic glass beads filter cake repelled most of the water during the dewatering process, thus showing that wettability plays a considerably important role in the filtration process as indicated by Asmatulu and Yoon (2012). In the case of the coal sample, small-diameter capillaries (Figure 4.1) were formed due to the presence of irregularly shaped particles.

The implementation of the 3D software capabilities of parallelization for the LBM simulation of multiphase fluid flow in porous media was successfully accomplished (Figures 5.1 through 5.6). The single component multiphase flow He-Chen-Zhang LBM model was extended to incorporate fluid-solid interaction forces, and was applied to the simulation of percolation in actual HRXMT images of pore network structures created by filtration experiments.

The pattern of percolation with viscous fingering type of flow was observed with more and longer fingers being formed for packed particle beds of hydrophilic glass beads. The instability was due to the stronger viscous interaction as revealed from 3D flow simulations. However, the pattern of percolation with capillary fingering type of flow with relatively short fingers was observed for packed particle beds of silica sand.

Due to the limitations in computing resources, only subsets of specific sizes were investigated. Improvements in this area are necessary to describe percolation behavior under different circumstances and larger volume sets. Future research efforts should include different strategies that allow for the computation of LBM simulations requiring different computing resources. This could lead to notable improvements in our understanding of filtration processes and the application of LBM simulations in different porous media.

APPENDIX A

SINGLE COMPONENT SINGLE PHASE LBM

The classical approach (Tiller, 1975; Dahlstrom & Silverblatt, 1977; Svarosvsky, 1990) for filtration analysis is based on Darcy's law, an empirical equation that describes one-dimensional fluid flow through uniform incompressible porous media. Knowledge of cake pore microstructure and its correlation to macroscopic cake properties is required to model the filtration from a fundamental point of view. Darcy's law is defined as:

$$U = \frac{Q}{A} = \frac{1}{A}\frac{dV}{dt} = \frac{k\,\Delta p}{\mu\,\ell} \tag{A.1}$$

where U is the fluid velocity (m/s), Q is the volume flow rate (m³/s), V is the volume of the fluid (m³), k is the permeability (m²), μ the dynamic viscosity of the fluid (Pa·s), A the cross-sectional area (m²) of the one-dimensional sample of length (or thickness of porous media) ℓ (m), and Δp is the pressure drop (Pa).

The single component, single phase LB model has been used as a common tool to study transport phenomena through pore space (Lin & Miller, 2004; Videla, Lin & Miller, 2007). In this regard, permeability was computed by modeling Stokes flow in both the simulated pore space of a packed bed and actual 3D digital pore space from HRXMT analysis using the LB method. Calculation of permeability is summarized here as follows.

For nonoverlapped spheres, the permeability k (unit of length^2) is related to the drag coefficient C_d,

$$k = \frac{\upsilon}{6\pi R C_d}$$ (A.2)

where υ is the unit cell volume, and R is the sphere radius.

For Darcy flow,

$$k = -\frac{U\mu}{dP/dx}$$ (A.3)

Compared with Equation A.2, U is the fluid velocity, average across an inlet or outlet face of the unit cell (including solids), μ is the dynamic viscosity, and dP/dx is the pressure gradient along the x-direction. Formally, the LB used in this study is a constant-pressure model, so the pressure gradient must be related to the body force. To relate the permeability to units measured in the LB simulation, a force balance was applied:

$$xBody\rho L^3 = (P_{in} - P_{out}) L^2 = -(dP/dx) L^3$$ (A.4)

or $(dP/dx) = -xBody\rho$, where L is the side of the simulation cell (in lattice units), $xBody$ is the body force, applied in the x-direction, per unit volume in the LB simulation, and ρ is the particle density per site specified in the LB simulation. Thus,

$$k = \frac{U\nu}{xBody}$$ (A.5)

where $\nu = \mu/\rho = (\tau - 1/2)/3$ is the kinematic viscosity specified in the LB simulation as shown in Equation A.2. Customarily k/L^2, normalized permeability, is reported rather than k to achieve scale-independence.

APPENDIX B

PHYSICS OF MULTIPHASE FLOW IN POROUS MEDIA

The flow of two immiscible fluids sharing simultaneously the complex pore space in porous medium is governed by the forces acting on the fluids, including pressure forces, viscous forces, gravity forces, inertia forces and interfacial surface forces (Videla, 2009). The relative importance of these forces is usually characterized by the Reynolds (Re), Bond (Bo), and Capillary (Ca) numbers, as well as the viscosity ratio (M) and these parameters are defined in Equations B.1 through B.4, respectively:

$$\text{Re} = \frac{u \cdot D}{v} \tag{B.1}$$

$$Bo = \frac{g(\rho_{nw} - \rho_w) \cdot R^2}{\gamma} \tag{B.2}$$

$$Ca = \frac{v_w \mu_w}{\gamma} \tag{B.3}$$

$$M = \frac{\mu_{nw}}{\mu_w} \tag{B.4}$$

In general, flow in porous media is dominated by the capillary forces, where inertia forces are negligible, and pressure forces and viscous forces are proportional to the rate of flow. Because the pressure forces and viscous forces depend on the flow rate, the

capillary forces and gravitational forces become more important when the rate of flow is slower.

B.1 Capillary Pressure

When two immiscible fluids are in contact in the porous medium a discontinuity in pressure exist across the interface (Videla, 2009). The difference in pressure is called the capillary pressure. The capillary pressure is defined as the difference between the pressures of the non-wetting fluid, p_{nw}, and the wetting fluid, p_w, as shown in Equation B.5:

$$p_c = p_{nw} - p_w \tag{B.5}$$

Figure B.1 shows a curved interface between two immiscible fluids under static equilibrium. From the figure it is observed that capillary pressure depends on the curvature of the interface. In soil science, the negative of the capillary pressure is known as tension or suction head.

Interfacial shapes in static and quasi-static situations are governed by the Laplace equation. By applying the condition of mechanical equilibrium of the forces acting on the interface, Laplace showed that the capillary pressure is proportional to the interfacial tension and inversely proportional to the curvature of the meniscus. Laplace's law is presented in Equation B.6 for a 3D pore structure and is dependent on the interfacial tension γ_{12} and the radii of curvature, r^*:

$$p_2 - p_1 = p_c = 2\frac{\gamma_{12}}{r^*} \text{ , with } \frac{1}{r^*} = \frac{1}{2}\left(\frac{1}{r'} + \frac{1}{r''}\right) \tag{B.6}$$
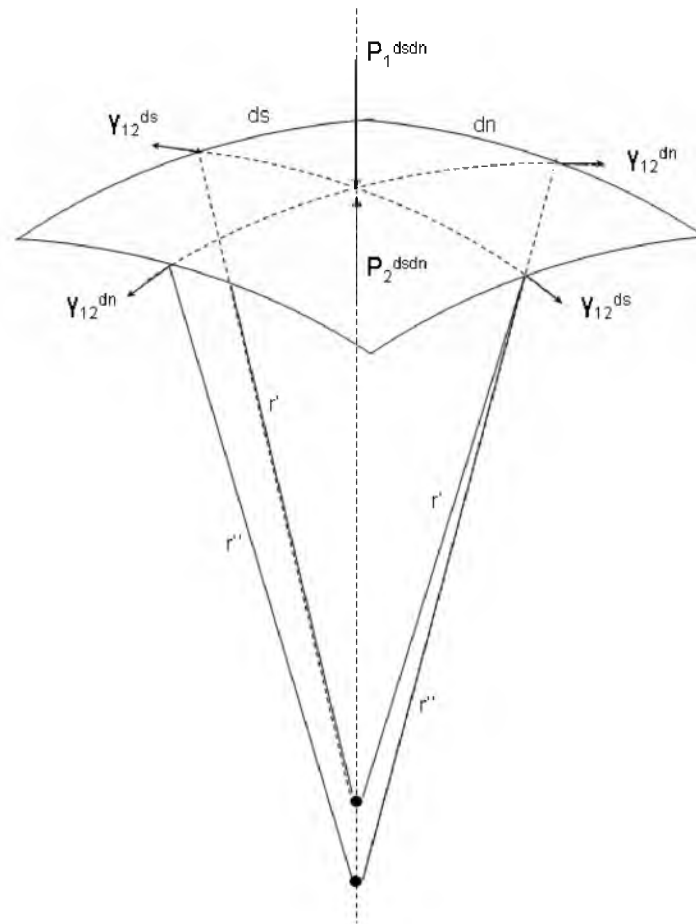
Figure B.1: Forces acting on the elementary surface around a point of a curved interface between two immiscible fluids at static equilibrium.

B.2 Interfacial Tension and Contact Angle

Porous structures involve the presence of a solid phase, which in a capillary system interacts with at least two fluids phases. As a result there are at least three surfaces subjected to surface tension as shown in Figure B.2.

The static equilibrium between the three interfacial tensions leads to the well known Young's equation as shown in Equation B.7:

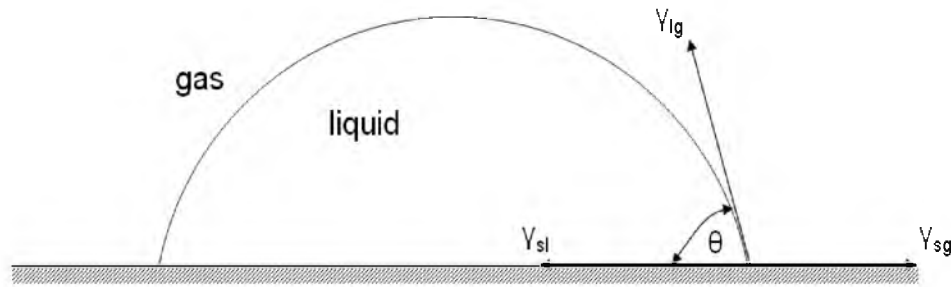$$\gamma_{lg} \cos \theta = \gamma_{sg} - \gamma_{sl} \tag{B.7}$$

Figure B.2: Static equilibrium between the three interfacial tensions at the solid surface.

The contact angle is normally used to describe the preferential characteristics of the solid surface to be wet. In some cases, no equilibrium is possible $(\gamma_{lg} > \gamma_{sg} - \gamma_{sl})$ and the liquid covers the whole surface completely, in such cases the liquid is said to wet the solid perfectly (Videla, 2009).

B.3 Capillary Pressure Versus Saturation Curves

The capillary pressure depends on the saturation, interfacial tension, wetting angle, viscosity ratio and Bond number (Marle, 1981). Because the capillary pressure depends on the contact angle one may expect a hysteresis effect, meaning that different capillary pressure – saturation curves are obtained depending on the history of the fluid motion. For example, the capillary pressure – saturation curve may depend on whether a sample was initially saturated with the wetting or nonwetting fluid component. If the sample is initially saturated with the wetting fluid an increment of the capillary pressure produces the displacement of the wetting fluid by the nonwetting fluid in a process known as drainage. If the sample is initially saturated with the nonwetting fluid, a decrease in the capillary pressure produces imbibition. Figure B.3 shows a typical curve

which reveals the relation of capillary pressure to saturation. The entry point, P^*, shows that if a sample is initially saturated by a wetting fluid a certain pressure must be built up before the nonwetting fluid begins to penetrate the sample; this is the so called threshold pressure or nonwetting entry value. The figure also shows that at high capillary pressure the wetting saturation reaches a minimum limit, this is the so called irreducible saturation of the wetting fluid, S_{w0}. The imbibition curve shows that a maximum limiting saturation value is reached at zero capillary pressure. This point corresponds to the residual saturation, S_{nw0}, of nonwetting fluids that stay entrapped in the porous solid. In the case of coal filtration, S_{nw0} represents the residual moisture in the cake at breakthrough. It is well known that pressure-saturation curves are subject to hysteresis phenomena, and therefore the capillary pressure is a function of the direction of displacement and the history of the two-phase flow in the porous sample.
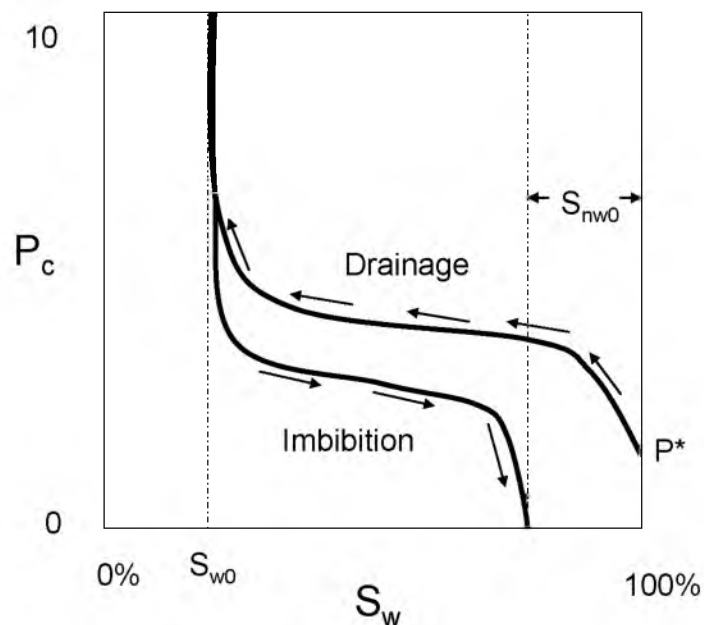

Figure B.3: Typical capillary pressure curve.

REFERENCES

Asmatulu, R., & Yoon, R. H. (2012). Effects of surface forces on dewatering of fine particles. Paper presented at the *Separation Technologies for Minerals, Coal, and Earth Resources*, 95-101.

Chen, H. (1993). Discrete Boltzmann systems and fluid flows. *Comput. Physics, 7*, 632-637.

Chen, S., & Doolen, G. (1998). Lattice-Boltzmann method for fluid flows. *Annu. Rev. Fluid Mech., 30*, 329-364.

Cormack, A.M., & Doyle, B.J. (1977). Algorithms for two-dimensional reconstruction. *Phys. Med. Biol., 22*, 994-997.

Dahlstrom, D.A., & Silverblatt, C.E. (1977). Continuous vacuum and pressure filtration. In D.B. Purchas (Ed.), *Solid Liquid Separation and Scale Up*. Croydon: Up Lands Press.

Ennis, B., Green, J., & Davis, R. (1994). The legacy of neglect in the U.S. *Chemical Engineering Progress, 90*, 31-43.

Frish, U., Hasslacher, B., & Pomeau, Y. (1986). Lattice gas automata for the Navier-Stokes equations. *Phys. Rev. Lett., 56*, 1505-1508.

He, X., Shan, X., and Doolen, G. (1998). Discrete Boltzmann equation model for non ideal gases. *Phys. Rev. E., 57*, R13.

He, X., & Doolen, G. (2002). Thermodynamics foundations of kinetic theory and Lattice-Boltzmann models for multiphase flow. *J. Stat. Phys., 107*, 309-328.

He, X., Chen, S., & Zhang, R. (1999). A Lattice-Boltzmann scheme for incompressible multiphase flow and its applications in simulation of Rayleigh-Taylor instability. *J. Comput. Phys., 152*, 642-663.

Hsieh, C.H. (2012). Procedure and analysis of mineral samples using high resolution x-ray microtomography. (Unpublished master's thesis). University of Utah, Salt Lake City.

ImageJ (2013). National Institutes of Health: ImageJ (Version 1.46) [Software]. Available from http://rsbweb.nih.gov/ij/download.html.

ImageJ Voxel Counter (2010). National Institutes of Health: ImageJ Voxel Counter [Software]. Available from http://rsbweb.nih.gov/ij/plugins/voxel-counter.html.

Isherwood, I. (2004). In memoriam: Sir Godfrey Hounsefield. *Radiology, 234*(3), 975-976.

Kang, Q., Zhang, D., & Chen, S. (2004). Immiscible displacement in a channel: Simulations of fingering in two dimensions. *Advances in Water Resources, 27*, 13-22.

Lenormand, R., Touboul, E., & Zarcone, C. (1988). Numerical methods and experiments on immiscible displacements in porous media. *J. Fluid Mech., 189*, 165-187.

Leonard, J.W., & Hardinge, B.C. (1991). *Coal Preparation, 5th Ed.*, Littleton, CO: Society for Mining, Metallurgy, and Exploration, Inc.

Lin, C.L., & Miller, J.D. (2004). Pore structure analysis of particle beds for fluid transport simulation during filtration. *Int. J. Miner. Process, 73*(2-4), 281-294.

Lin, C.L., Miller, J.D., Videla, A. R., & Mejia, J. A. (2010). Fine coal filtration as revealed by 3D Lattice-Boltzmann simulations. *International Journal of Coal Preparation and Utilization, 30*, 217-238.

Lindquist, W. B. (2009). 3DMA-Rock: A software package for automated analysis of pore rock structure in 3D computed microtomography images. Retrieved from http://www.ams.sunysb.edu/lindquis/3dma/3dma_rock/3dma_rock.html.

Lindquist, W.B., Lee, S., Coker, D.A., Jones, K.W., and Spanne, P. (1996). Medial axis analysis of void structure in three-dimensional tomographic images of porous media. *Journal of Geophysical Research, 101*(B4), 8297–8310.

Marle, C.M. (1981). *Multiphase Flow in Porous Media.* Houston: Gulf Publishing Company.

Novelline, R. (1997). *Squire's Fundamentals of Radiology.* 5th Edition. Harvard University Press.

ParaView (2007). Kitware, Sandia National Labs and CSimSoft: ParaView (Version 3.0) [Software]. Available from http://paraview.org/paraview/resources/software.php.

Rothman, D.H., & Zaleski, S. (1997). *Lattice-gas cellular automata: Simple models of complex hydrodynamics.* Cambridge, UK: Cambridge University Press.

Shan, X., & Chen, H. (1993). Lattice-Boltzmann model for simulating flows with multiple phases and components. *Phys. Rev. E,. 47*, 1815-1819.

Succi, S. (2001). *The Lattice-Boltzmann equation for fluid dynamics and beyond.* New York: Oxford University Press.

Sukop, M.C., & Thorne, D.T. (2006). *Lattice-Boltzmann modeling: An introduction for geoscientists and engineers* (First Ed.). New York: Springer.

Svarosvsky, L. (1990). Filtration fundamentals. In L. Svarosvsky (Ed.), *Solid-liquid separation.* London: Butterworths.

Tien, C. (2006). *Introduction to Cake Filtration.* New York: Elsevier.

Tiller, F.M. (1975). Compressible cake filtration. In K. Ives (Ed.), *Scientific Basis of Filtration,* London: Noordhoff.

Videla, A.R. (2009). Explorations in three-dimensional Lattice-Boltzmann simulation for fluid flow in packed particle bed. (Unpublished doctoral dissertation). University of Utah, Salt Lake City.

Videla, A.R., Lin, C.L., & Miller, J.D. (2007). Simulation of saturated fluid flow in packed particle beds: The Lattice-Boltzmann method for the calculation of permeability from XMT images. *Journal of the Chinese Institute of Chemical Engineers, 39,* 117-128.

VolSuite (2009). Ohio Supercomputer Center (OSC): VolSuite (Version 3.3.20) [Software]. Available from http://archive.osc.edu/supercomputing/software/apps/volsuite.shtml.

Wakeman, R., & Tarleton, S. (2005). *Principles of industrial filtration.* New York: Elsevier.

Wildenschild, D., & Sheppard, A. P. (2013). X-ray imaging and analysis techniques for quantifying pore-scale structure and processes in subsurface porous medium systems. *Advances In Water Resources, 51,* 217-246

Xradia. (2012). Retrieved from http://www.xradia.com.

XRadia. (2012). *MicroXCT-200 and MicroXCT-400 User's Guide.* Retrieved from http://www.xradia.com/products/microxct-400.php.

Yoon, R.-H., J. Salomon, M. K. Eraydin, J. Zhang, S. Keles, and G. H. Luttrell. (2006). Development of advanced fine coal dewatering technologies. XV Int. Coal Prep. Cong. Beijing, China, October 17–20, 2006, 1: 575–583.

Zhang, R., He, X., & Chen, H. (2000). Interface and surface tension in incompressible Lattice-Boltzmann multiphase model. *Computer Physics Communications, 129,* 121-130.